Nutritional status assessment of olive crops by means of the analysis and modelling of multispectral images taken with UAVs

Miguel Noguera [1]*, Arturo Aquino [1], Juan Manuel Ponce [1], António Cordeiro [2], José Silvestre [2], Rocío Calderón [2], Maria da Encarnação Marcelo [2], 'Pedro Jordão [2] and José Manuel Andújar [1]

[1] Centro de Investigación en Tecnología, Energía y Sostenibilidad (CITES), Universidad de Huelva, La Rábida, Palos de la Frontera, 21819 Huelva, Spain; miguel.noguera@diesia.uhu.es (M.N.); arturo.aquino@diesia.uhu.es (A.A.); jmponce.real@diesia.uhu.es (J.M.P.); andujar@diesia.uhu.es (J.M.A.)

[2] Instituto Nacional de Investigação Agrária e Veterinária, I.P. (INIAV), Herdade do Reguengo, Elvas, Portugal; antonio.cordeiro@iniav.pt (A.C.); jose.silvestre@iniav.pt (J.S.); rocio.arias@iniav.pt (R.C.); encarnacao.marcelo@iniav.pt (M.E.M.); pedro.jordao@iniav.pt (P.J.)

* Correspondence: miguel.noguera@diesia.uhu.es; Tel.: +34 959 21 77 20

Abstract. This research was aimed at developing an efficient method for Nitrogen, Phosphorus, and Potassium (NPK) foliar content retrieval in olive trees by means of the analysis and modelling multispectral images taken by an unnamed aerial vehicle (UAV) under field conditions. To this end, an experiment was carried out in a super hight density olive orchard. The fertirrigation system of the experimental area was sectorized to obtain plots with different status of NPK. The orchard was overflown with a UAV equipped with a multispectral camera that photographed the entire experimental surface. A new image analysis approach was developed for integrating all the spectral images gathered during the flight in orthomosaics from which to automatically extract information from discrete points. Finally, several retrieval techniques (partial least squares regression, artificial neural network (ANN), support vector regression and Gaussian process regression) were evaluated for NPK leaf content retrieval by using the spectral data as input variables, and the results of chemical analyses as reference. Among all, the best results were obtained by ANN approach (N (R^2 = 0.63), P (R^2 = 0.89), K (R^2 = 0.93)). These results showed the suitability of the proposed image processing approach and indicate ANN as the best recovery technique for the experimental conditions evaluated. However, the approach must be validated under other environmental conditions, olive varieties and plant vegetative stages before making fertilization recommendations.

Keywords: Multispectral; nitrogen; phosphorus; potassium; Artificial Neural Network (ANN); Unmanned Aerial Vehicle (UAV); precision agriculture

1. Introduction

The olive tree (*Olea europaea L.*) is one of the main perennial crops in Mediterranean agriculture and play an important role in the international agricultural landscape. The gastronomic qualities of olive oil and table olives have made them key elements in the Mediterranean diet which, in 2013, was declared Intangible Cultural Heritage of Humanity by UNESCO.

In 2018, the area cultivated with olive crops in the European Union accounted for more than 5 Mha, with a production of 13.7 Mt of olives (65% of the worldwide yield) (FAOSTAT, 2020). In order to increase the productivity of the crops, in the last decades, hedgerow olive orchards with high plant densities (>1500 trees ha^{-1}), or super high densities (2116 trees ha^{-1}.) have increased dramatically. The elevated number of plants per area increases the evaporative demand of the whole crop, so an exhaustive fertigation management is required.

Under this context, precision agriculture techniques are being introduced in the sector, resulting in modern olive orchards which are usually drip-irrigated, fertirrigated, kept under no-tillage techniques to overcome soil erosion problems, harvested by mechanic means and quick-growing methods for young olive plantings (López-Granados, Jurado-Expósito, Álamo, & García-Torres, 2004). However, farmers still manage fields as if they were homogeneous surfaces. We argue that this is a mistaken approach, as there are a lot of factors (soil properties, plot morphology, pathologies, microclimate, etc) that are heterogeneously distributed in the field and determine the effectiveness in the plants resources consumption.

Fertilization is one of these factors, which is essential for plant growth and yield. The mineral nutrients most applied in agriculture are Nitrogen (N), Phosphorus (P) and Potassium (K) ("FAOSTAT," 2020). The actual plant uptake of each nutrient is very variable in terms of space and time. However, farmers generally manage fertilization homogenously, based on the application rates of fertilizers in intuitive and visual practices. Thus, fertilization is often oversupplied. The excess of fertilizers not uptake by the plants can leach or become lost through run-off, accumulating in natural water bodies. This leads to

severe ecological effects, such as algal blooms or eutrophication of freshwater lakes and coastal areas (R. Fernández-Escobar et al., 2009; Savci, 2012). On the one hand, excessive fertilization causes plant stress, which in turn renders the plants susceptible to diseases (Bindraban, Dimkpa, Nagarajan, Roy, & Rabbinge, 2015; Sanzani, 2012) and cause problems related to production (R. Fernández-Escobar et al., 2006) . On the contrary, insufficient fertilization also derives in a variety of problems for crops. In general N, P, or K deficiencies negatively affect photosynthetic assimilation and crop yield, both in terms of quantity and quality (Hank et al., 2019; López-Granados et al., 2004).

The consideration of crops as homogeneous surfaces to make decisions regarding fertilizer application, stems from the limitations of traditional nutrient status assessment techniques. These methods require leaf sample collection and tedious chemical analysis (Sui, Wilkerson, Hart, Wilhelm, & Howard, 2005). Thereby, they are destructive, time-consuming, expensive and provide incomplete information since sampling is based on limited sites in each field (Ali, Al-Ani, Eamus, & Tan, 2017). Thus, the varying degrees of heterogeneity across the entire field are not usually represented (Camino, González-Dugo, Hernández, Sillero, & Zarco-Tejada, 2018; López-Granados et al., 2004). For reaching optimal yield from an economic and environmental side, fertilizers application rates should be determined by considering the actual uptake rates of the crop (Lemaire, Jeuffroy, & Gastal, 2008). Therefore, it is necessary to consider new approaches, which increase the spatial and temporal resolution of the current methods. The possibility of mapping the variability of entire crops would enable the adaptation of fertilizer applications to the necessities of each part of the field. This would contribute to increase the efficiency of current fertilization programs (Saberioon, Amin, Gholizadeh, & Ezri, 2014).

In the last decades, numerous researchers have focused their interest in spectral image to characterize biophysical parameters of vegetation and, concretely, nutritional status (Berger et al., 2020; Hank et al., 2019; Verrelst et al., 2019). This research line is based on the fact that the three processes of absorption, reflection and transmission describe interactions between incident radiation, leaf biochemical constituents and canopy biophysical traits. Thus, by characterizing the interaction

between light and canopy, it is possible to develop predictive models of vegetation parameters of interest (Li, Li, Yao, Li, & Liu, 2020). Moreover, the use of UAVs for data acquisition allows to cover vast field areas with a minimal effort, providing the method with an unprecedented spatial and temporal resolution (Mondino, 2018). These resources have enabled the emergence of multiple new applications of UAVs for monitoring several crop parameters of interest for decision making, such as: water status (Gonzalez-Dugo et al., 2013; Park et al., 2017), detection of weeds and pathogens (Calderón, Navas-Cortés, Lucena, & Zarco-Tejada, 2013), yield prediction (Barzin, Pathak, Lotfi, Varco, & Bora, 2020), growth vigour assessment (Caruso et al., 2019), and nutrient status (Liu, Zhu, & Wang, 2017).

To the best of our knowledge, most of research aimed to develop non-destructive methods for plant nutrient status assessment based on spectral image acquired with UAV, have been focused on Nitrogen (N), with other important nutrients scarcely discussed, especially for olive trees. In this sense, Gómez Casero et al., (2007) evaluated a method aimed to monitor N and P deficiency in olive trees by means of hyperspectral image acquired manually from above the tree. Their approach was based on the widely accepted normalized difference vegetation index (NDVI) and just allowed to make a qualitative distinction between olive trees under deficiency and olive trees under good condition (Gómez-Casero et al., 2007). More recently, Lee et al., (2020) carried out a study aimed at using UAV equipped with multispectral cameras to predict canopy's nitrogen concentration in corn fields. They evaluated linear regression, random forests, and support vector machine models to predict N weight from individual multispectral bands (475-840 nm)(Lee et al., 2020). In another work, Perry et al., (2018) evaluated a set of vegetation indices based on spectral bands (550-810 nm) acquired with an UAV at canopy-scale for leaf %N estimation in a red-blush pear orchard (Perry, Goodwin, & Cornwall, 2018). They proposed a new index (Modified Canopy Chlorophyll Content Index) reaching R^2 of 0.67 and RMSE of 0.24 % between the estimated and the reference values. Liu et al., (2017) evaluated a multifactor statistical regression and a back propagation neural network approach for leaf nitrogen content (LNC) estimation in a winter wheat study at different growth stages. They informed of varying accuracy at

different growth stages for both models. The neural network approach yielded generally better results than those given by the multiple linear regression modelling (Liu et al., 2017).

On the other hand, most of the few studies have focused on the estimation of phosphorus (P) and potassium (K) were carried out under laboratory conditions on a leaf scale. In this sense, Zhang et al., (2013) used hyperspectral imaging (380-1030 nm) coupled with non-linear least-squares support vector machines to map the distribution of leaf N, P and K content (LNC, LPC and LKC) in oilseed rape (Zhang, Liu, He, & Gong, 2013). The model's performance produced R^2 values of 0.88 for LNC, 0.71 for LPC, and 0.75 for LKC. In another work, Malmir et al., (2020) used a visible-near infrared (400–1000 nm) hyperspectral imaging system to predict LNC, LPC and LKC of cocoa trees. They used partial least squares regression (PLSR) models to predict leaf nutrients concentrations, with a prediction accuracy in terms of R^2 of 0.74, 0.75 and 0.35 for LNC, LPC and LKC, respectively (Malmir, Tahmasbian, Xu, Farrar, & Bai, 2020). Pandey et al., (2017) preformed an *in vivo* study intended to quantify LNC, LPC and LKC of maize and soybean. They used a hyperspectral imaging system (550-1700 nm) coupled with an automated conveyor belt system for spectral data collection. PLSR were used as mathematical models, yielding the following performance for the three nutrients (N (R^2= 0.92, RMSE=0.41); P (R^2= 0.83, RMSE=0.056); K (R^2= 0.83, RMSE=0.41)) (Pandey, Ge, Stoerger, & Schnable, 2017). On the other hand, Wang et al., (2020) used hyperspectral imaging (908–1735 nm) to predict LPC and LKC in tea plants. They evaluated different pre-processing methods and several mathematical approaches to determine the nutrients' concentration through spectral data. The best performance was obtained by using multiple linear regression models with R^2 and RMSE values of 0.94 and 0.093 for LPC, and 0.92 and 0.494 for LKC (Y. J. Wang et al., 2020).

The aim of this research is to improve the state of the art, developing an efficient method for the recovery of NPK canopy content in olive trees from multispectral images obtained with UAV under field conditions. For that, the fertirrigation system of an experimental olive grove was divided into sectors to obtain plots with different conditions of LNC, LPC and LKC. This experimental field was

overflown with an UAV equipped with a commercially available five-band multispectral camera that photographed the entire experimental surface. A new approach to image analysis was developed with a double aim: 1) integrating all the spectral images collected during the flight in orthomosaics, and computing a digital surface model (DSM); 2) deriving a region of interest (ROI) by segmenting olive canopies from the background by exploiting elevation information contained in the DSM using mathematical morphology techniques. The computed ROI, then allowed to accurately and automatically extract multispectral reflectance information from discrete points. Finally, several retrieval techniques including PLSR, artificial neural network (ANN), support vector regression (SVR) and gaussian process regression (GPR)) were evaluated for NPK leaf content estimation by using the multispectral reflectance data automatically extracted from the orthomosaics as input variables, and the results of chemical analyses as reference.

The main novelty of this job is that offers evidence that olive tree LPC and LKC monitoring by means of spectral data acquired under field conditions may be viable. To the best of our knowledge, most of attempts in the development of non-destructive methods for plant nutrient status assessment by means of spectral data have been centred on modelling N foliar content. In fact, most of the few studies focused on LPC and LKC estimation have been accomplished under laboratory conditions at leaf scale (Malmir et al., 2020; Pandey et al., 2017; Y. J. Wang et al., 2020; Zhang et al., 2013). In this sense, the proposed image processing methodology is an essential part of the approach, which determine the accuracy of the spectral information zenithally acquired from the air under field conditions. This is due to this image processing allows to isolate the canopy pixels discarding the background information by exclusively using a digital surface model (DSM). Thus, the followed approach is able to accurately segment olive canopies being robust against the presence of shadows, weed or other common distractors. Moreover, it should be stressed that, contrary to other solutions, the one presented in this paper could be potentially affordable for small-scale growers, as it does not make use of expensive sensors like LiDAR or hyperspectral devices, nor heavy unmanned aerial vehicles.

157 Hereafter, the present manuscript is structured as follows: Section 2 focuses on the experimental
158 design. Thus, Section 2.1 describes the characteristics of the experimental field and the protocol
159 design. Section 2.2 exposes all the aspects related to how aerial image acquisition was performed.
160 Section 2.3, describes the processing of the individual images taken during a flight mission, aimed at
161 extracting accurate multispectral information specifically from olive canopies. Then, Section 2.4
162 describes the methodology used to derive an estimation of the nutritional status of the orchard in
163 terms LNC, LPC, and LKC by means of the acquired multispectral information. Section 3 presents the
164 results obtained, which are then discussed in Section 4. Section 5 concludes the manuscript, giving a
165 summary of the main findings achieved and identifying aspects that might be approached in further
166 investigations.

167 **2. Materials and methods**

168 **2.1 Study site description, and experimental field protocol design**

169 The experiment was carried out with two varieties of *Olea europaea L.* – Arbequina and Arbosana -
170 established in olive groves located in Elvas, district of Portalegre (Alentejo, Portugal). The first plot,
171 centred in the coordinates 7˚08'08''W and 38˚49'20.5''N as illustrated in Fig. 1-(a), has an approximate
172 area of 64.9 ha, and cultivates the Arbequina variety under a super intensive scheme. It has a plant
173 spacing pattern of 1.35 m x 3.75 m (inter and intra-row, respectively). The second plot, represented in
174 Fig. 1 (b), cultivates the Arbosana variety and is located at the coordinates 7˚07'25.9''W and
175 38˚50'06.9''N, and also implements a super intensive plant spacing pattern of 1.35 m x 3.75 m,
176 resulting in 2116 trees/ha.

177 The applied fertilization is controlled in the fertigation system with periodic adjustment of the nutrient
178 application rates based on the phenological phase of the annual cycle. The nutrients requirements to
179 be applied are calculated based on the results of the chemical analysis of leaves and the estimate of
180 the olives production. Weeds in the experimental site are mechanically controlled. The orchard's soil
181 has a heterogeneous composition, with a predominance of loam and sandy-loam areas, however there

182 are some clay-loam zones in the northern area of the orchard. This irregular pattern in terms of the
183 composition of the soil is also reflected in the values of electrical conductivity (CEa). Most of the zones
184 present low and medium CEa values, except for specific areas with highest CEa values. Regarding
185 acidity, the pH of the soil was between 7 and 8.

186 According to the Köppen–Geiger classification, the climate of the study area is Csa (hot-summer
187 Mediterranean climate), with an average annual rainfall of approximately 600 mm, concentrated from
188 October to May and mostly outside a 4-month summer drought period. In the spring and summer,
189 when inflorescences / flowering / fruit set, fruit growth and fat accumulation occur, irrigation is
190 necessary to obtain an acceptable yield, as rainfall and water reserves in the soil are not sufficient to
191 meet the needs of the plants. These orchards were equipped with a drip irrigation system to supply
192 water and nutrients during water stress periods, until autumn (September / October), coinciding with
193 the beginning of the rainy season. The fertigation scheme consisted of daily drip irrigation calculated
194 weekly according to evapotranspiration and adjusted to the phase of the phenological cycle.

195 The experimental field design was established with three modalities: control - normal fertigation (NF)
196 - company scheme; and two modalities with regulated deficit: medium stress (RDF_1), with 61% of
197 normal fertigation and moderate stress (RDF_2), with 50% of normal fertigation. In each olive grove
198 we randomly selected three lines of trees for each modality (with minimum of 50 olive trees / row),
199 and in different places where we selected four olive trees for sampling, a total of twelve olive trees per
200 modality. A boundary with 4 lines was also established next to each olive line where the same
201 procedure was applied.

202 The modalities of regulated deficit in fertigation for 2019 - NF, RDF_1 and RDF_2 - started on July 19th
203 (dominant phenophase endocarp hardening) and ended on September 18th (the beginning of the rainy
204 season). According to this schedule, the NF period lasted 62 days and, in the modalities, RDC_1 and
205 RDC_2 there was a reduction of 23 days and 31 days, respectively.

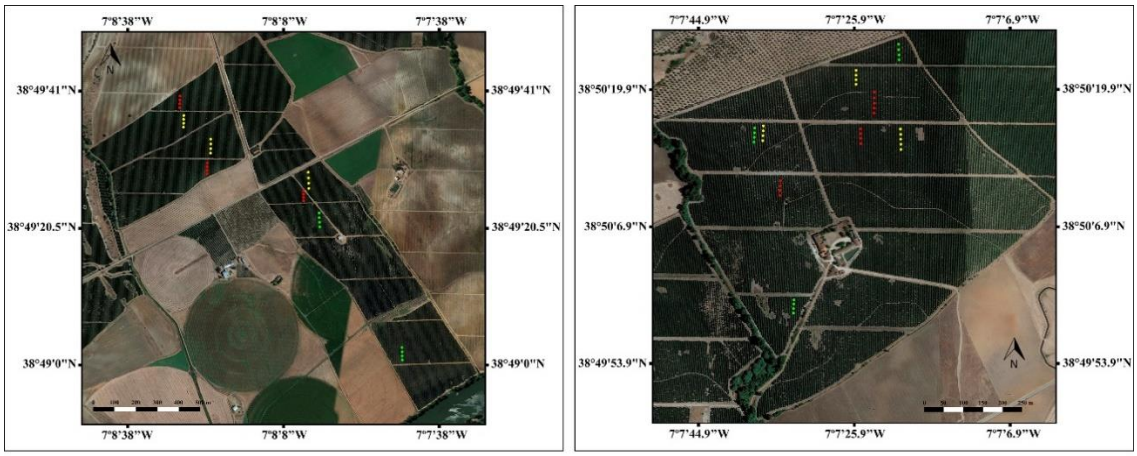

206

207 **Fig. 1.**- Cultivars used for experimentation, one of the Arbequina variety (a) and the other one
208 (b) cultivating the Arbosana variety. Green, yellow and red dots represent respectively represent
209 normal fertigation (NF), medium stress (RDF_1) and moderate stress (RDF_2).

210 **2.2 Image Acquisition**

211 **2.2.1 Equipment**

212 The two plots under study were sampled using a DJI™ Matrice 100 (SZ DJI Technology Co., Ltd.,
213 Shenzhen, Guangdong, China) unmanned aerial vehicle (UAV), equipped with a MicaSense RedEdge-
214 M™ (MicaSense, Inc., Seattle, WA, USA) multispectral camera (see Fig. 2). This camera includes five
215 CMOS sensors, each of them with modified sensitivity thanks to band-pass filters which make them
216 individually sensible to narrow bands within the visible spectrum (VIS), blue, green, red, and red-edge
217 and near-infrarred (NIR) bands of the spectrum, respectively. All the sensors are 1280 × 960 pixels in
218 size, which results in a ground sample distance (GSD) of around 8 cm per pixel when capturing at an
219 elevation of 120 m. The camera was powered with a GPS device, which allowed image georeferencing,
220 and a 5-band downwelling light sensor (DLS) which, along with the use of a reflectance panel, enabled
221 to perform radiometric calibration (Micasense Support, 2020).

222 Tables 1 and 2 summarize the main features of the DJI™ Matrice 100 and the MicaSense RedEdge-
223 M™, respectively.

224 **Table 1**

225 Main features of the DJI™ Matrice 100 unmanned aerial vehicle (UAV).

Type	Quadcopter
Diagonal Wheelbase	650 mm
Max Take-off Weight	3600 g
Max Speed	17 m/s (GPS mode, no payload, no wind) 22 m/s (ATTI mode, no payload, no wind)
Max Wind Resistance	10 m/s
Operating Temperature	-10° to 40°

226 **Table 2**

227 Main features of the MicaSense RedEdge-M™ multispectral camera.

Spectral Bands	Centre Wavelength (nm)	Bandwidth (nm)
Blue	475	20
Green	560	20
Red	668	10
Red-Edge	717	10
NIR	840	40
Ground Sample Distance (GSD)	~8 cm per pixel (per band) at 120 m AGL[1]	
Max Capture Rate	1 capture per second (all bands), 12-bit RAW	
Field of View	47.2° HFOV[2]	
Imager Resolution	1280 × 960 pixels	

228 [1] Above Ground Level.

229 [2] Horizontal Field of View.

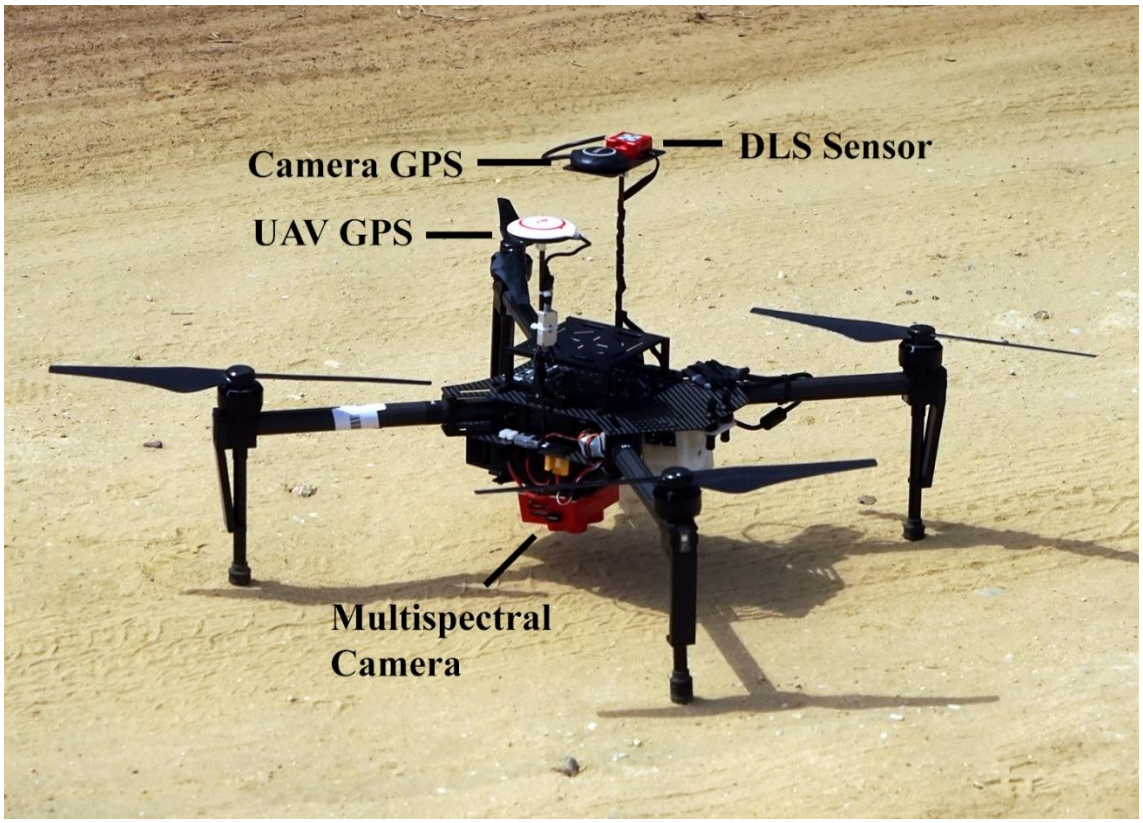

Fig. 2.- Aerial platform used for multispectral image acquisition.

2.2.2 Flight Planning and Execution

Flights over the olive orchards were planned a-priori by using the DJI™ Flight Planner software (AeroScientific- Spatial Scientific Pty. Ltd., Adelaide, Australia). Due to the vast extension of the plots considered in the study, and the availability of a flight-time autonomy of around 15 min, five and six flight plans were required to completely cover the "Arbequina" and "Arbosana" plots, respectively. All flight plans shared the same configuration, aiming at capturing aerial images with a forward overlap of 85% and a lateral overlap of 65%, at a flight altitude and cruising speed of 100 m (which corresponded to a GSD of around 6.5 cm/pixel) and 35 km/h, respectively; images were taken every 1.5 s. Flights were executed autonomously in GPS mode and monitored with the ground control software Litchi (VC Technology Ltd.©, London, UK).

The Arbosana plot was sampled on September 10, 2019, approximately between 11:30 and 16:00; 3,122 images were taken per each of the five spectral bands (15,610 in total). The Arbequina plot was

flown on the next day, according to the same timetable, thus capturing 3,055 images per band (15,275 in total).

Table 3 summarizes the main settings and outcomes of the flight sessions, whereas Fig. 3 shows an example of the same scene captured during a flight mission in the blue, green, red, red-edge and NIR spectral bands.

Table 3

Summary of the main settings and outcomes of the flight missions developed on September 10 and 11, 2019, to sample the Arbosana and Arbequina plots.

	Arbosana	Arbequina
Area Covered	64.9 ha	85.8 ha
Nº of Flights	6	5
Forward Overlap	85%	
Side Overlap	65%	
Flight Altitude	100 m	
Cruise Speed	35 km/h	
Ground Sample Distance (GSD)	~6.5 cm/pixel	
Frame Rate	1/1.5 image/s	
Nº of Images Captured	15,610 (3,122 per band)	15,275 (3,055 per band)

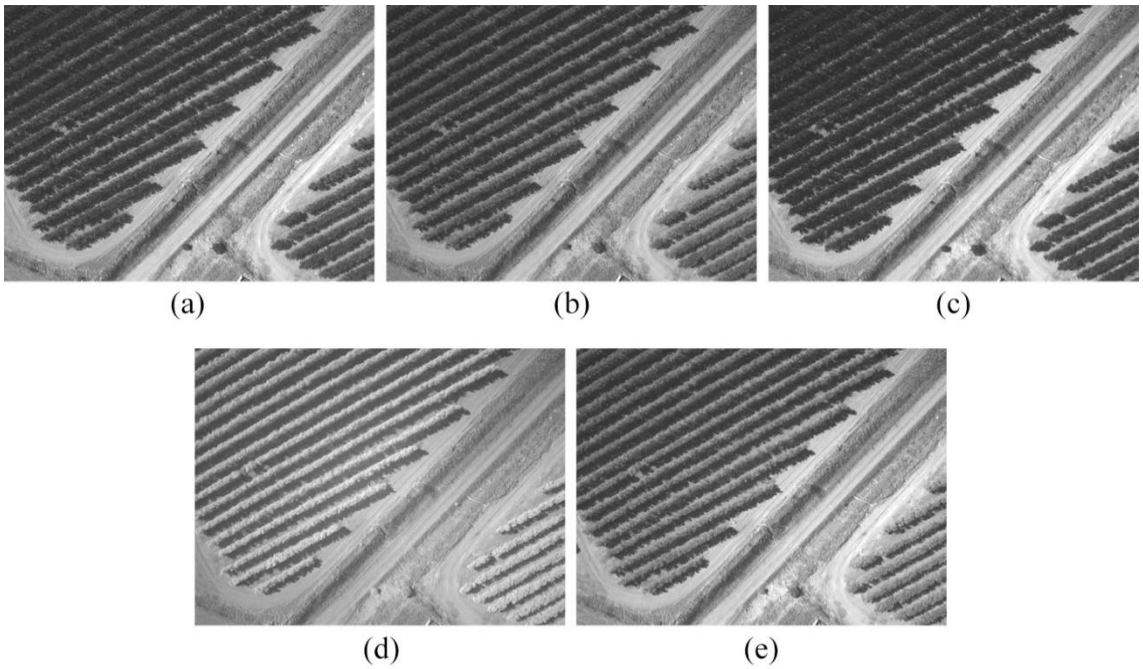

253

254 **Fig. 3.-** Example of an aerial image captured in the five considered spectral bands: (a) blue; (b) green;
255 (c) red; (d) red-edge; (e) near-infrared (NIR).

256 **2.3 Image processing methodology for the automated extraction of accurate olive-trees spectral**
257 **information**

258 The developed methodology to estimate nutritional status of olive orchards can be divided into two
259 main blocks. The first block comprises the processing of the individual images taken during a flight
260 mission, aimed at extracting accurate multispectral information specifically from olive canopies. Once
261 this information is available, the second phase is focused on modelling this multispectral information
262 to derive an estimation of the nutritional status of the orchard in terms of nitrogen, phosphorus, and
263 potassium. Fig. 4 offers a flowchart diagram illustrating the main phases of the outlined methodology.

264

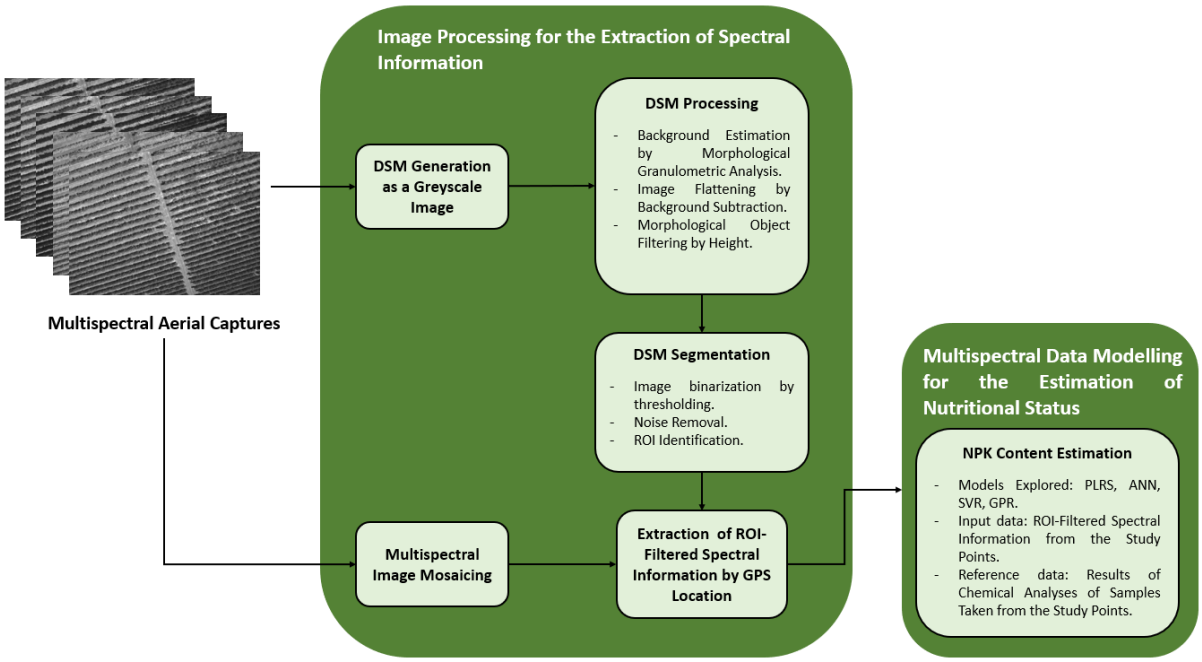

Fig. 4.- Flowchart diagram of the proposed methodology for the estimation of nutritional status of olive orchards from aerial multispectral image analysis and modelling.

2.3.1 Image Processing for the Automated and Accurate Extraction of Spectral Information

For a given georeferenced canopy pixel, this stage describes a methodology aimed at automatically calculating its representative spectral information captured in the images corresponding to the five bands studied. To obtain this representative information, canopy pixels closely surrounding the given location are considered, discarding from this selection those pixels representing other disturbing elements likely to be present in the images, such as forage. To perform this filtering robustly, a region of interest (ROI) is applied, which is computed by morphologically exploiting information contained in a digital surface model.

With the exception of some initial processing described in section 4.1.1., which is there specified, the methodology described throughout this paper was implemented using the Matlab R2019b platform and its Image Processing and Deep Learning toolboxes, release 2018a (The Math-Works Inc., Natick, Massachusetts, USA). The methodology makes extensive use of Mathematical Morphology operators, so the reader is encouraged to study their fundamentals if needed (Soille, 2004).

2.3.2 Multispectral Image Mosaicing and DSM Generation

For each of the five spectral bands, an image mosaic is built by matching the individual images taken during a flight mission, which are previously radiometrically corrected (Micasense Support, 2020) using the illumination information registered by the camera's DLS sensor and the reflectance measured in the images captured of the reference board. In parallel, a 3D point cloud associated to the orthomosaics is generated as well, in which an elevation value is decided for those pixels which are automatically identified in, at least, three different individual images. In these cases, a point associated to the pixel in the orthomosaics is added to the cloud, and its elevation with respect to the sea level, expressed in metres, is estimated by combining GPS information with that yielding from re-projecting the pixel in the individual images in which it was identified. These procedures were carried out using the photogrammetry Pix4D™ Mapper software (Pix4D S.A., Prilly, Switzerland).

Then, a greyscale image representing a digital surface model, DSM, of the orthomosaics is generated from the 3D point cloud. To that end, pixel values in image DSM are set to the elevation values of their spatially corresponding points in the cloud, when this information is available. For those pixels corresponding to points in the cloud with unresolved elevation, their values are decided by applying inverse distance weighting (IDW) interpolation (Shepard, 1968), which estimates the elevation of a given pixel from the known elevation values of pixels in its surroundings. The influence of these surrounding pixels in the calculation decreases as their distance from the pixel under evaluation increases. Thus, if p_0 represents an unresolved pixel in image DSM, its elevation value $DSM(p_0)$ is interpolated under the IDW principles as follows:

$$DSM(p_0) = \sum_{i=1}^{N} \lambda_i DSM(p_i) \quad (1)$$

where $DSM(p_i)$ stands for the known elevation of the *i*-th surrounding point p_i, and λ_i is the weight assigned to p_i, which varies according to its distance with respect to p_0 as follows:

$$\lambda_i = \frac{d_{i0}^{-x}}{\sum_{i=1}^{N} d_{i0}^{-x}} \quad (2)$$

x is a weighting exponent modelling the way in which weight decreases with distance. Weights λ_i vary between 0 and 1, additionally fulfilling that their total sum is the unit: $\sum_{i=1}^{N} \lambda_i = 1$. For the experiments described in this paper, a surrounding circle of a radius of 2.5 m around the points to be interpolated was considered, this to prevent that elevation of canopy points to be inferred were mainly influenced by ground points and vice versa. This effect was strengthened by only considering $N = 4$ closest points in the neighbour. The weighting exponent x was set to 2.

Fig. 5 shows the digital surface model computed for the arbequina plot following the described methodology. It should be noted that, as image DSM contains values of altitude with respect to the sea level, the minimum number of bits required for its codification may vary depending on the elevation of the area under study. For the case of this research, 8 bits were sufficient.

2.3.3 DSM Processing

The aim of the image processing methodology specified in this section is to transform image DSM to favour its subsequent binarization. This segmentation is aimed at deriving a ROI allowing the accurate discrimination between pixels from the olive canopies and the background.

The first step consists in homogenising the grey level values of DSM to avoid information regarding ground elevation. Indeed, DSM's pixel values represent altitude magnitudes with respect to the sea level. Thus, pixels of olive trees located at low altitudes, may have lower grey level values than those of ground pixels placed at higher altitudes; this effect can be checked in Fig. 5. To favour olive trees segmentation despite their absolute elevation, DSM is homogenised by subtracting from it a background estimate:

$$DSM_h = DSM - DSM_{BG} \quad (3)$$

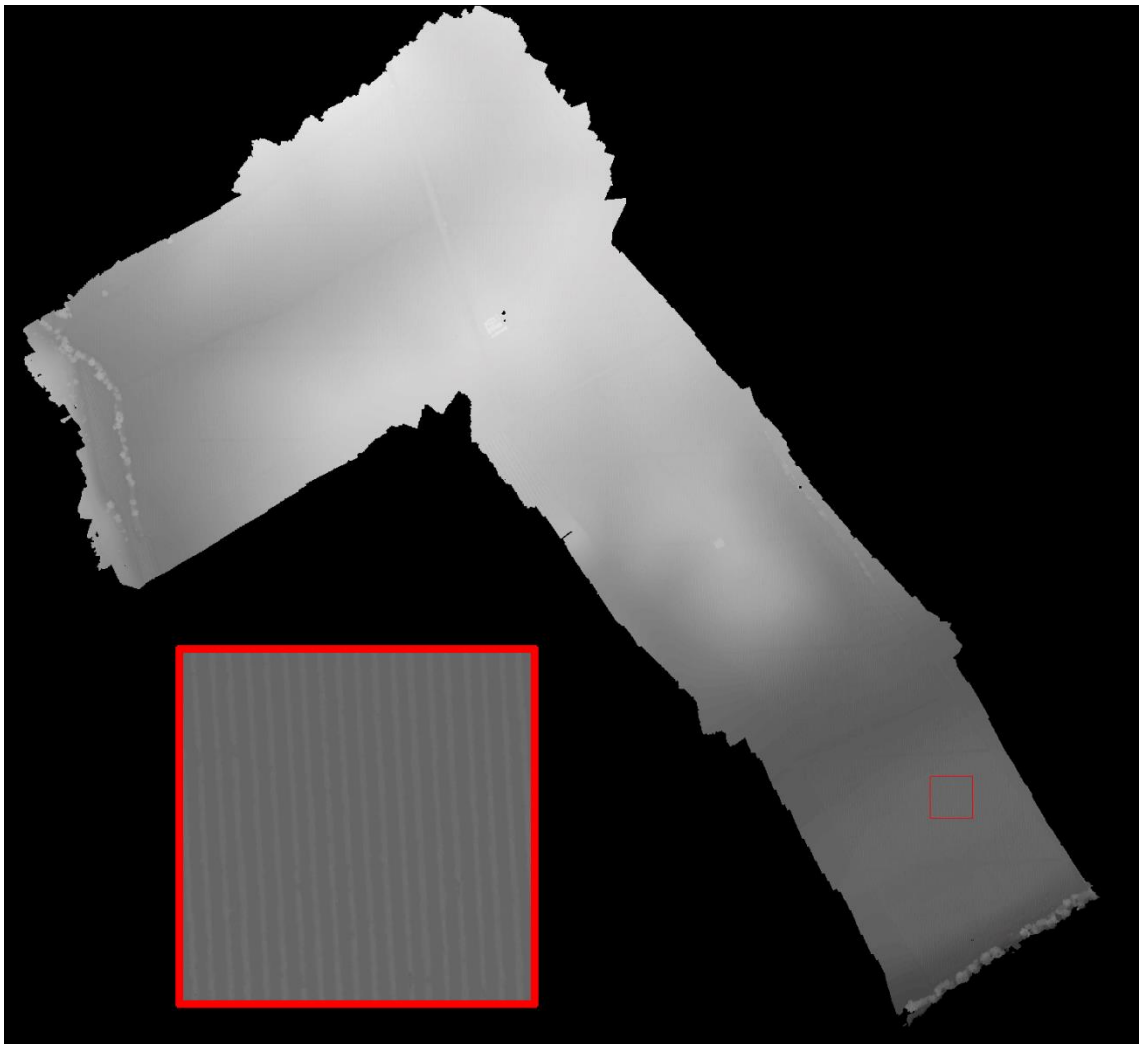

Fig. 5.- Representation of the digital surface model, image DSM, computed for the arbequina plot; image display range is expanded for the sake of facilitating its visualisation. Pixel values represent altitude values expressed in metres, so brighter pixels indicate higher altitudes. Note how the orography of the plot is represented, and also check in the zoomed area highlighted in the red square, how rows of olive trees appear brighter, i.e. elevated, with respect to their surroundings.

Background estimate DSM_{BG} is calculated by iteratively applying the morphological operator opening (γ) to DSM, using a circular structuring element of increasing radius, and assigning to the minimum value given by the set of opening operations to every pixel. Thus, any given pixel (x, y) of image DSM_{BG}, mathematically fulfils that:

$$DSM_{BG}(x,y) = \left\{ \left[\gamma_{\beta_i}(SMD)\right](x,y) \middle| \left[\gamma_{\beta_i}(SMD)\right](x,y) \leq \left[\gamma_{\beta_j}(SMD)\right](x,y), i,j = 1,\dots,n \right\} \quad (4)$$

β_i is a circular structuring element of radius i pixels, and n is the maximum radius value considered. The optimum filtering of olive rows pixels takes place when their grey level values are substituted, thanks to the opening operation, with the minimum value existing in their close background neighbourhood. It happens when the operation is performed using a structuring element with the minimum radius allowing the element to overflow the row, which usually happens in the dimension of width. Thus, the maximum radius value of β_i, n, must be high enough to allow the structuring element to overflow any row existing in the image, at the time that it also keeps the area covered by the element being meaningfully local. The fact that row width is not expected to exceed more than a few metres (it is even controlled by pruning), and the unlikeliness of olive orchard surfaces having dramatic variations in elevation such as those produced by cliffs, provides a wide margin to set a value for n respecting the described precepts. In the case of the orchards analysed in this paper, a value of $n = 10$ pixels is set, which is equivalent to 0.75 m for the spatial resolution of 0.0769 m per pixel managed in this study (this resolution is conditioned by camera features and flight altitude).

The approach formulated in eq. (4), provides a flexible framework favouring the accurate filtering of every row independently from its size. The subtraction of the background image calculated with this method, DSM_{BG}, from image DSM, produces an image DSM_h in which the original surface is ideally flattened and placed at the sea level. Fig 6 illustrates the result of this effect.

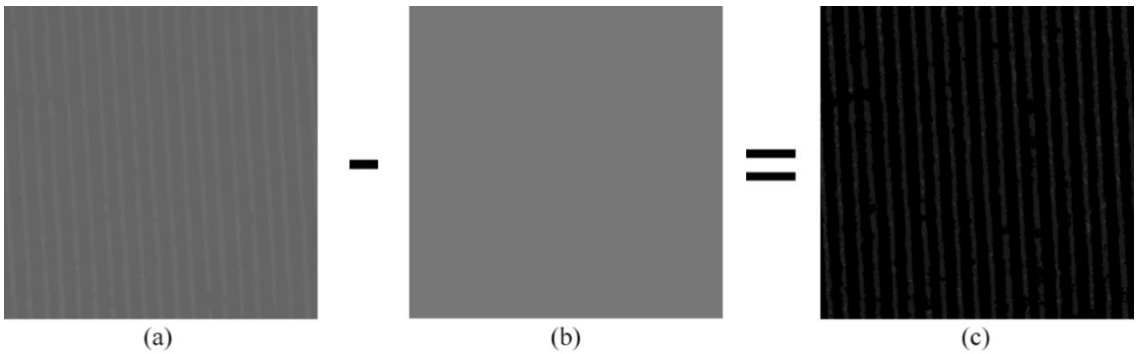

(a) (b) (c)

Fig. 6.- Representation of the process of homogenising image DSM: (a) zoomed area of DSM represented in Fig. 5; (b) background estimation of image (a) by applying eq. (4); (c) result of the homogenisation of (a) by applying eq. (3). Note that contrast of the represented images has been improved to enhance their visualisation.

With the designed processing method, olive canopies are the elements expected to have higher grey level values in DSM_h; this is, they are the ones expected to be the tallest elements in the image. The next stage in the processing is aimed at removing regional maxima considered as irrelevant from DSM_h, which were those pixel aggregations with altitude values lower or equal than 1.5 m. It is achieved by applying the *H*-maxima transform to image DSM_h:

$$DSM_{h\_filt} = HMAX_h(DSM_h) = R^{\delta}_{DSM_h}(DSM_h - h), h = 1.5 \quad (5)$$

where R^{δ} represents the morphological reconstruction by dilation (δ) of DSM_h from marker $DSM_h - h$. In this case, those regional maxima having elevation values greater than 1.5 m were retained for being considered of interest; note that this criterion can be easily adjusted by modifying the h parameter.

2.3.4 DSM Segmentation

Image DSM_{h_filt}, obtained by means of filtering by height in eq. (5), is now binarized by using the threshold Th_{Otsu} provided by the Otsu's thresholding method [4]:

$$DSM_{bin}(x,y) = \begin{cases} 255, if\ DSM_{h_{filt}}(x,y) > Th_{Otsu} \\ 0, \quad in\ any\ other\ case \end{cases} \quad (6)$$

Next, a morphological opening is applied to the binary image DSM_{bin} to remove eventual spurious connected components (set of neighbour foreground pixels) that are abnormally small, thus not representing olive canopies:

$$DSM_{bin}{}' = \gamma_{\beta}(DSM_{bin}) \quad (7)$$

where γ_β represents the morphological opening applied by using a circular structuring element of 5 pixels in radius. The choice of the circular shape for the structuring element responds to the fact that it is the most effective one to remove noise, as connected components of any shape can be completely covered by the element if the length of its maximum axis is lower or equal than the diameter of the element. Additionally, the radius value was empirically set to remove connected components with an extremely abnormal tiny size. To recover the exact shape of the connected components surviving this noise filtering, and thus yielding the final ROI, DSM_{bin} is morphologically reconstructed by dilation (R^δ) from marker $DSM_{bin}{}'$:

$$ROI = R^{\delta}_{DSM_{bin}}(DSM_{bin}{}') \quad (8)$$

Note that this operation makes the choice of the size of the structuring element used in eq. (7) not critical, as the impact of the operation with moderate larger elements in the surviving connected components is restored by the morphological reconstruction.

See Fig. 7 to check the computed ROI.

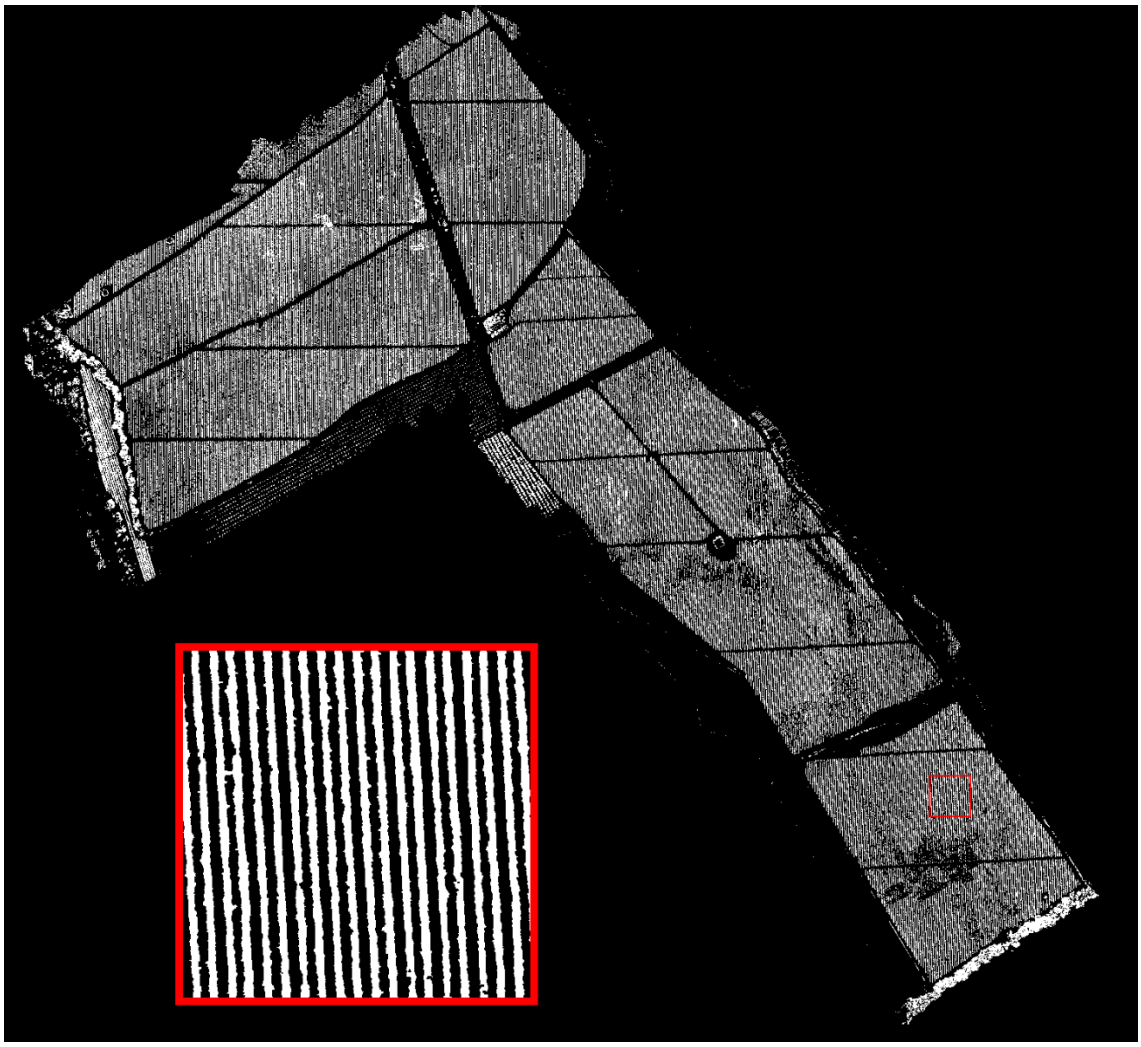

Fig. 7.-Computed region of interest (ROI) which*, as it can be corroborated in the zoomed red-squared image,* accurately delimits olive-tree canopies.

2.3.5 Extraction of ROI-Filtered Spectral Information by GPS Location

At this point, five orthomosaics (one per spectral band) and a ROI delimiting olive canopies have been yielded for the two plots under study. The interest now is to calculate a representative spectral response in each band for a given olive canopy geolocation. As canopies have a certain degree of porosity, the geolocated point is not considered to be representative. Thus, for each band, this representative spectral response is decided as the average response given strictly towards canopy pixels (filtered using the ROI) contained in a square neighbourhood, centred in the pixel of interest, of size $0.5m \times 0.5m$, which corresponds to a size in pixels of 7×7.

2.4 Methodology for nutritional status estimation from multispectral information

2.4.1 Analytical Methods

In this work, leaf nitrogen, phosphorus, and potassium content (LNC, LPC and LKC) were defined as target parameters since they are widely accepted indicators of the nutritional status evaluation of olive orchards (Fernández-Escobara, 2018). These three parameters represent the content of the mentioned mineral elements in a given leaf mass, determined by different chemical methods. Olive trees require the essential mineral elements in suitable levels or may suffer from their lack or excess. Generally, inadequate status of N, P or K in olive trees results in negative effects on productivity and quality of the yield. In fact, tissue analysis, and in particular leaf analysis, is a standardized method that is regularly used for the management of crops fertilization programs. The interpretation of leaf analyses allows to determine the application rates of each fertilizer based on its actual levels. The best time to perform it is in the summer, 5 to 8 weeks after full flowering, due to the levels of most nutrients in the olive leaf stabilizing during this period (Barranco Navero, Diego, Fernandez Escobar, Ricardo, Rallo Romero, 2017). Notwithstanding, this current scheme is inefficient due to the leaf samples are manually collected, as well as it is also inaccurate, as the number of samples taken is very poor in terms of spatial resolution, which results in a lack of representativity of the whole orchard, in which many sources of variability can be present.

A total of 70 leaf samples from two different olive varieties were used in this research, including 35 of Arbequina and 35 of Arbosana, collected in September coming from two distinct areas. On the flight day, a sample of 100±20 g of leaves was collected from each sampled point, from the middle of the last spring terminal shoots. The samples were placed in plastic bags and rapidly taken to the laboratory, where they were refrigerated for a subsequent chemical analysis.

The leaf samples were washed with distilled water, dried at 65±5 °C and ground to a particle size of 1±0.1 mm.

LNC was determined by the Kjeldahl method:~500 mg of ground material was digested in tubes with Kjeldahl catalyst tablets and 10 ml concentrate sulphuric acid, thus converting nitrogen compounds into ammonium sulphate. The temperature program followed in the digest block was 30 minutes at 185 °C and 60 minutes at 410 °C. After adding 50 ml of 40 % sodium hydroxide to the digestion solution, the produced ammonium was evaporated by distillation as ammonia. This was condensed in the cooling system and flows into a conical flask with 20 ml of 2% boric acid solution. This solution was analysed for ammonia by titration with 0.025 M hydrochloric acid (Vogel, 1978).

For the analysis of LPC and LKC, ~500 mg of ground material was reduced to ashes in a muffle at 500±10 °C over four hours. The ashes were solubilised in hydrochloric acid 3 M. LPC and LKC were determined in the resulting solution by inductively coupled plasma optical emission spectrometry (ICP-OES) (Chaves et al., 2010; Duarte, Pacheco, & Soveral-Dias, 1998; Thompson, 2012).

The results refer to dry material at 100-105 °C.

2.4.2 Setting up training and external validation sets

The experimental field was considered as a whole, not differentiating between olive varieties, looking to increase the volume and the range of the dataset. The range of the data covered the upper and lower tolerance limits in the three cases (NPK). Nevertheless, the values were heterogeneously distributed, with a greater distribution near the lower limit of tolerance.

In this study, leaf samples (n=70) were divided into a calibration dataset (n=53) and a validation dataset (n=17). The training dataset was used to calibrate the models, and the external validation dataset was employed to test performance of these models. Due to the heterogeneous distribution of the dataset, the training and external validation sets were manually configured for the training set to cover the whole range of the data for the three nutrients, being the validation set ranges included in the training set ranges. This configuration resulted in the presence of a similar ratio of sample points of both olive varieties (Arbequina and Arbosana) in both sets. Table 1 summarizes the statistical details of the training and validation sets used for each nutrient.

Table 4

Statistics for the olive tree LNC, LPC and LKC for the training and validation dataset.

	Set	n	Range	Mean	SD
N	Training	53	1.24 -2.14	1.59	0.21
	Validation	17	1.25 – 2.01	1.62	0.18
P	Training	53	0.06 – 0.25	0.11	0.04
	Validation	17	0.06 – 0.20	0.10	0.04
K	Training	53	0.16 – 1.22	0.55	0.25
	Validation	17	0.17 – 0.81	0.53	0.20

2.4.3 Retrieval methods

In this work, the five items of spectral data extracted from UAV-captured images were used as input variables. Thus, one linear nonparametric regression method (partial least squares regression (PLSR)) and three nonlinear non-parametric methods (artificial neural network (ANN), support vector regression (SVR) and gaussian process regression (GPR)) were evaluated as retrieval techniques. All these approaches were implemented using the Matlab software (MathWorks, Natick, MA, United States).

2.4.3.1 Partial least squares regression (PLSR)

PLSR has been widely used in precision agriculture applications. This data-driven approach uses mathematical and statistical methods to extract information from complex data. The method increases the value of the data by transforming them into new features (Geladi & Kowalski, 1986; Verrelst et al., 2019). Concretely, PLSR is a bilinear calibration approach which reduce the large amount of measured collinear spectral variables to non-correlated principal components by using data compression. These data represent the relevant structural information that can be used to predict the dependent variable.

460 The mentioned features make PLSR a suitable method for the retrieval of vegetation biophysical
461 parameters trough spectral information, especially when predictors present multicollinearity and
462 when the number of measured wavelengths is higher than the number of observations (Wold,
463 Sjöström, & Eriksson, 2001).

464 **2.4.3.2 Artificial neural network (ANN)**

465 An ANN is a nonlinear non-parametric method (machine learning method). This approach consists on
466 a structure of neurons connected to each other and organized in layers. The neurons of different layers
467 are interconnected, and each connexion has a specific weight. Each neuron fundamentally
468 accomplishes a linear regression followed by a nonlinear function. Briefly, the ANN architecture works
469 to minimize the mean-square deviation trough the error-correction learning rule. Thereby, the error
470 will be reduced by adjusting the weight of each layer of neurons. These features result in an
471 extraordinary ability to link complex spectral information with key parameters without any constraints
472 on the sample distribution. This makes ANN approaches suitable for defining the intricate nonlinear
473 relationships that normally exist between canopy-level spectral signatures and biophysical
474 parameters.

475 To determine the optimum configuration of the ANN, several settings were evaluated varying the
476 number of hidden layers and the number of neurons. The best setting was selected based on the
477 changes in RMSE and R^2 between the response of the model and the reference values. Finally, the most
478 simplistic architecture of the net was selected, which comprised one hidden layer with one neuron,
479 five inputs (each reflectance value captured by the spectral sensor employed) and one output (LNC,
480 LPC and LKC respectively). The Levenberg-Marquardt algorithm was selected as the training algorithm
481 for being considered the most suitable according to the volume and the range of the dataset and the
482 processing capabilities of the computer used for training the models. Training was automatically
483 stopped when generalization stopped improving, as indicated by an increase in the mean square error
484 of the internal validation samples taken from the training set.

2.4.3.3 Support vector regression (SVR)

SVR belongs to other group of machine learning methods, concretely, Kernel-based regression methods. This method accomplishes a linear prediction model over mapped samples to a much higher dimensional space, which is associated in a nonlinear way with the original input space. Thus, the kernel function transforms the non-linear data boundaries in an original data space into linear ones in the higher dimensional feature space. SVR is based on the theory of support vector machine (SVM). The use of a structural risk minimization principle instead of empirical risk minimization, gives SVM the capacity of minimizing a bound on the risk function, rather than minimizing the error in training data. Additionally, SVM are not affected by collinearity, as it is a projection method where the input data are first projected on to a higher dimensional space before they are employed in the estimation process (Morlini, 2006). All of these offers SVM a good balance between the model's complexity and its generalization ability.

In this study, linear, quadratic, and cubic kernel functions were tested in SVR analysis. Then, the linear function was selected. The optimal values of free SVR parameters were determined based on a five folds cross validation.

2.4.3.4 Gaussian process regression (GPR)

GPR is also a kernel-based method, which is founded on a Bayesian formalism and thus implies a formal treatment of uncertainty quantification and error propagation. In GPR, the training phase takes place in a Bayesian framework, which implies probabilistic outputs (Camps-Valls et al., 2016). As a probabilistic approach, this model is trained to determine individual functions to all training data by fitting a mean and a covariance function (Pasolli, Melgani, & Blanzieri, 2010).

In this study, the model hyper-parameters were automatically optimized by maximizing the marginal likelihood in the training set. Several kernel functions (rational quadratic, squared exponential, matern 5/2 and exponential) were evaluated. Finally, the exponential function was selected.

509 **2.4.4 Criteria for model performance evaluation**

510 The performance of models was measured by the coefficient of determination (R^2) and the root mean
511 square error (RMSE), between the reference values of leaf nutrient content obtained by chemical
512 analysis and the responses of each model for the different nutrients (NPK). The smaller RMSE and
513 greater R^2 indicate the better performance of models.

514 **3. Results**

515 **3.1 Nutritional status of sampled and spectral data**

516 A total of 70 leaf samples from two olive trees varieties were used in this research, including 35 of cv.
517 Arbequina and 35 of cv. Arbosana. The chemical analyses revealed unequal trends according to the
518 three nutrients considered. In the case of N, significant differences were observed between olive trees
519 exposed to different fertirrigation treatment. This trend was similar in the case of P. On the other hand,
520 in the case of K, a real effect of fertirrigation treatments on nutrient status was not observed.
521 Nevertheless, considering the experimental field as a whole, a clear difference between olive varieties
522 related to the leaf content of P and K was observed. Generally speaking, olive trees of cv Arbosana
523 showed lower levels of both nutrients than those of cv Arbequina. Since both varieties received the
524 same fertirrigation scheme, the differences in nutrient status might be due to the differences in
525 physical or chemical characteristics of the soil of both plots. Surely, the heavier texture of the
526 Arbequina plot's soil might have a restraining influence on mineral nutrient leaching compared to that
527 of the Arbosana plot, thus resulting in a higher nutrient availability (Tremblay, Fallon, & Ziadi, 2011).
528 For this reason, and aimed at increasing the volume of the dataset, the sample points of the two olive
529 varieties (35 of Arbequina and 35 of Arbosana) were considered as a whole.

530 Thus, considering both plots together, the foliar analyses (n = 70) indicated that LNC varied between
531 1.24 and 2.14 %, with an average concentration of 1.60 ± 0.2 %. On the other hand, LPC varied between
532 0.06 and 0.25 %, with an average concentration of 0.10 ± 0.04 %. Finally, the LKC varied between 0.16
533 and 1.22 %, with an average concentration of 0.54 ± 0.2%. Figure 8 represents LNC, LPC and LKC in

each sampled olive tree and the levels of nutritional status. In the case of N, most of the sampled olive trees (76.8 %) presented an appropriate LNC, within the range 1.4–2.0 % (Fernández-Escobara, 2018), 7.2% of individuals showed LNC values above the upper limit (2.0 %) and only a 16 % presented LNC values below the critical level of 1.4 %. In regard to P, all the olive samples presented an appropriate LPC, within the range 0.05–0.3 % (Fernández-Escobara, 2018), but it was observed a trend towards the deficient limit. In the case of K, a 31.9 % of the sampled trees showed subcritical values below 0.4 %, 11.6 % of individuals showed LKC values above the adequate limit (0.8 %), and the remaining 56.5 % presented suitable LKC values within the range between 0.4-0.8% (Fernández-Escobara, 2018). The general trend towards the lower limit could be due to the sample collection date, as the standard reference limits were established with information collected on the hardening of the endocarp, whereas our results were observed on leaves collected two months after that period.

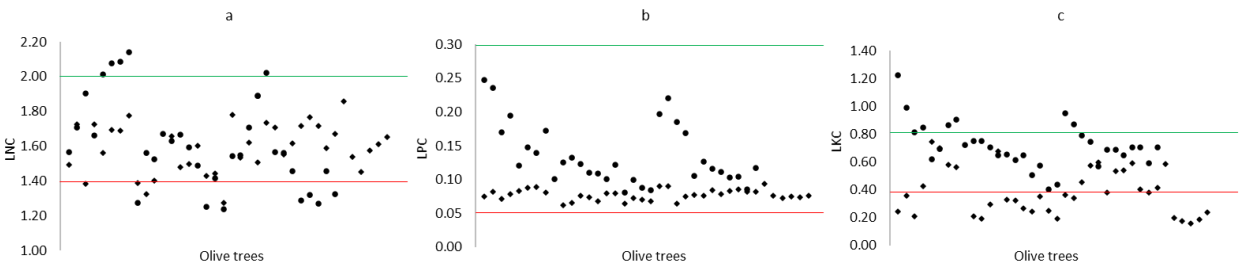

Fig. 8.- LNC (a), LPC (b) and LKC (c) of sampled olive trees (n = 70) and nutritional levels. The red line represents the deficient limit and the green line the adequate limit according to reference values based on olive leaves collected on the hardening of the endocarp phenophase (July) (Ricardo Fernández-Escobar, 2019) . Dots and diamonds represent single sampled trees of cv. Arbequina and Arbosana, respectively.

Figure 9 represents the mean reflectance curves of the olive trees under suitable and subcritical levels of LNC, LPC and LKC, respectively (in the case of P, it was considered a hypothetical limit of 0.08%). Overall shapes were similar throughout the wavelengths measured, although in the cases of P and K was observed a similar pattern. This trend was characterized by small increases of canopy reflectance in the olive trees under subcritical levels of nutrients for all the measured bands. These reflectance

peaks were especially noticeable at 550 and 700 nm and to a lesser extent at 670 nm. In the case of N, there weren´t significant differences between the canopy reflectance of the olive trees under suitable levels of LNC and the olive trees under subcritical levels for the five measured bands.

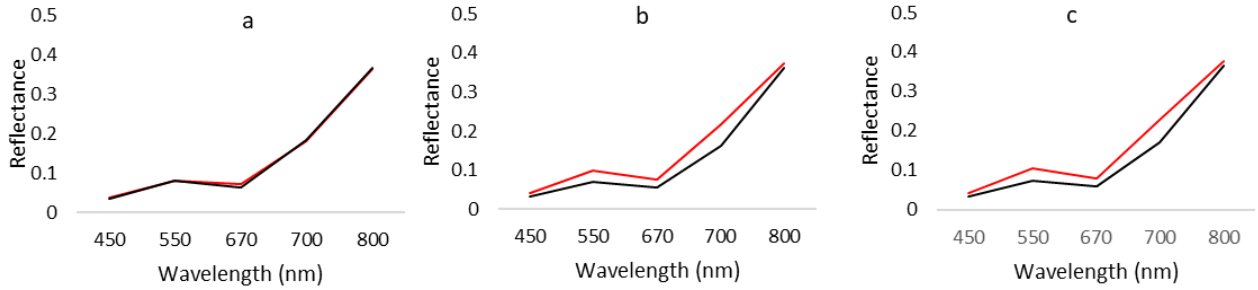

Fig. 9.- Meant reflectance curves of olive trees under suitable (black) and subcritical levels (red) of LNC (a), LPC (b) and LKC (c).

3.2 Evaluation and Comparison of the Robustness of the ANN, PLSR, SVM and GPR approaches

The spectral data extracted from each orthomosaic (one per spectral band) understood as the average response given towards canopy pixels contained in a standardized area, were used as input for training the ANN, PLSR, SVM and GPR approaches. In this section, the performance of the four retrieval methods is compared.

Figure 10 shows the changes in RMSE and R^2 as a function of the number of hidden neurons in the prediction of the LNC, LPC and LKC by means of ANN approaches.

The results indicated that with just one hidden neuron, the response of the model was accurate enough, yielding goodness-of-fit with LNC (R^2 = 0.63; RMSE = 0.117), LPC (R^2 = 0.89; RMSE = 0.013) and LKC (R^2 = 0.93; RMSE = 0.053). The increase in the number of hidden neurons did not constitute a significant improvement in the accuracy of the model. In the case of LNC prediction, a small increase of the R^2 value was observed when the number of hidden neurons was 9, but it came accompanied by an increase in RMSE (R^2 = 0.66; RMSE = 0.130). On the other hand, as for LPC estimation, there was also an increase in R^2 when the number of hidden neurons was 3, but it again supposed an increase in RMSE (R^2 = 0.90; RMSE = 0.014). Finally, in the case of LKC prediction the best performance was

reached with just one hidden neuron. Considering the rising RMSE and the greater complexity of the models as the number of hidden neurons was increased, it was selected an architecture with one hidden layer with a unique neuron for the ANN analyses based on canopy spectra.

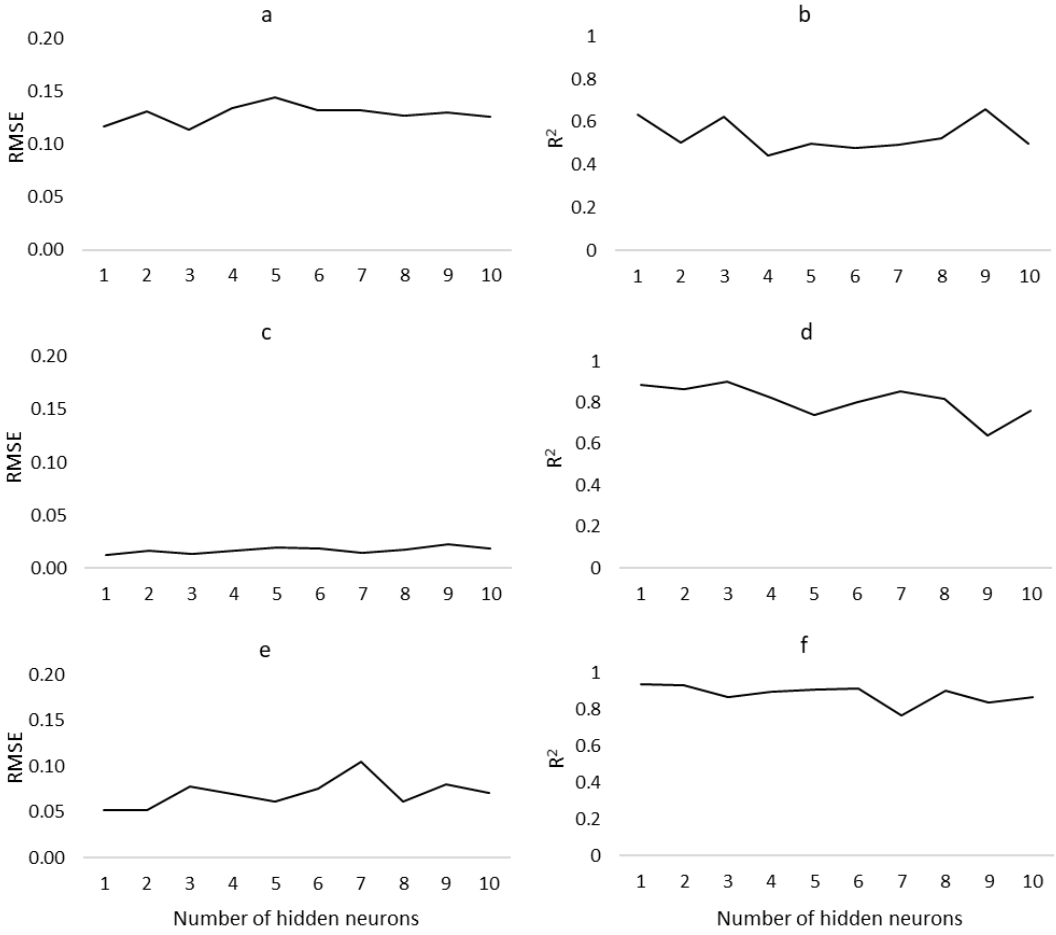

Fig. 10.- Changes in RMSE and R^2 as a function of the number of hidden neurons for LNC (a and b), LPC (c and d) and LKC (e and f) estimation for the ANN approaches.

Regarding to SVM, several kernel functions were tested (linear, quadratic, and cubic). Among all the linear function was selected for its best yield. On the other hand, as for GPR analysis various kernel functions (rational quadratic, squared exponential, matern 5/2 and exponential) were also evaluated. Finally, the exponential function was selected due to its performance.

When comparing the robustness of the four evaluated retrieval methods, a clear difference in performance was observed for LNC estimation against LPC and LKC, regardless the approach tested.

Concretely, the prediction of the canopy LNC yielded the worst results for all the proposed models. The coefficients of determination (R^2) of the linear regressions between the LNC measured by chemical methods and the response of the models were 0.63, 0.29, 0.38 and 0.19 for ANN, PLSR, SVM and GPR approaches, respectively (Table 5). The trend was similar according to the values of RMSE, for which the ANN approach yielded 0.117, the PLSR 0.248, SVM 0.146 and GPR 0.169 (Table 5). These results indicated that, despite the generally poor trend, the ANN model reached a greater accuracy related to LNC estimation when compared to the rest of the models.

Contrary, the prediction of LPC and LKC showed promising results for the four models evaluated. Again, the best results for both nutrients were obtained through the ANN approach with coefficients of determination (R^2) of 0.89 and 0.93 and values of RMSE of 0.013 and 0.052 for LPC and LKC prediction, respectively (Table 5). The response of the PLSR, SVM and GPR models were worse according to all the metrics considered. The PLSR approach yielded better results for LPC prediction with coefficients of determination (R^2) of 0.80, against the 0.71 reached for the SVM and the 0.67 reached for GPR. In terms of RMSE the trend was similar, with values of 0.017, 0.025 and 0.024 for PLSR, SVM and GPR approaches, respectively (Table 5). On the other hand, for LKC estimation, SVM, PLSR and GPR showed similar performances, with coefficients of determination (R^2) of 0.80, 0.80 and 0.79 and values of RMSE of 0.101, 0.115 and 0.089 respectively (Table 5).

Table 5

R^2 and RMSE between LNC, LPC and LKC measured through chemical methods and those estimated values based on PLSR, ANN, SVM, and GPR.

	LNC		*LPC*		*LKC*	
	R^2	**RMSE**	**R^2**	**RMSE**	**R^2**	**RMSE**
PLSR	0.29	0.248	0.80	0.017	0.80	0.115
ANN	**0.63**	**0.117**	**0.89**	**0.013**	**0.93**	**0.052**
SVM	0.38	0.146	0.71	0.025	0.80	0.101
GPR	0.19	0.169	0.67	0.024	0.79	0.089

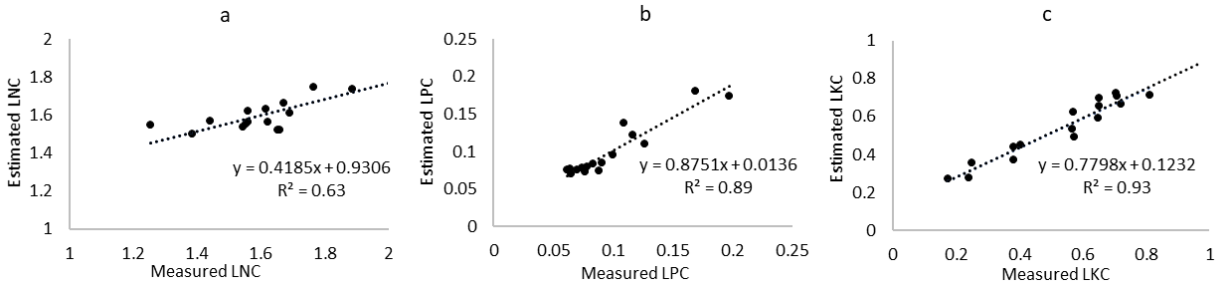

609

610 **Fig. 11.-** Linear regressions between LNC (a), LPC (b) and LKC (c) measured through chemical methods

611 and those estimated values based on ANN.

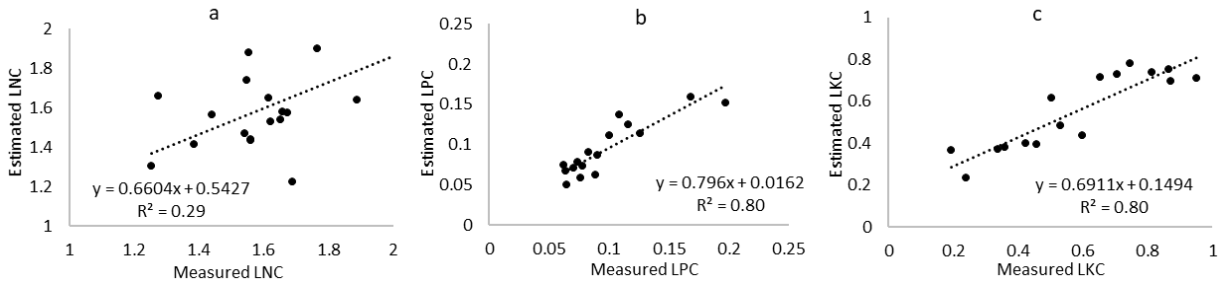

612

613 **Fig. 12.-** Linear regressions between LNC (a), LPC (b) and LKC (c) measured by chemical methods and

614 those estimated values based on PLSR.

615

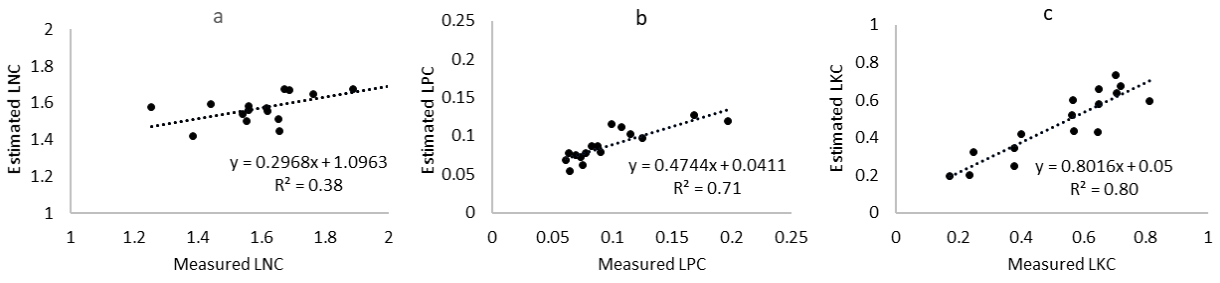

616

617 **Fig. 13.-** Linear regressions between LNC (a), LPC (b) and LKC (c) measured by chemical methods and

618 those estimated values based on SVM.

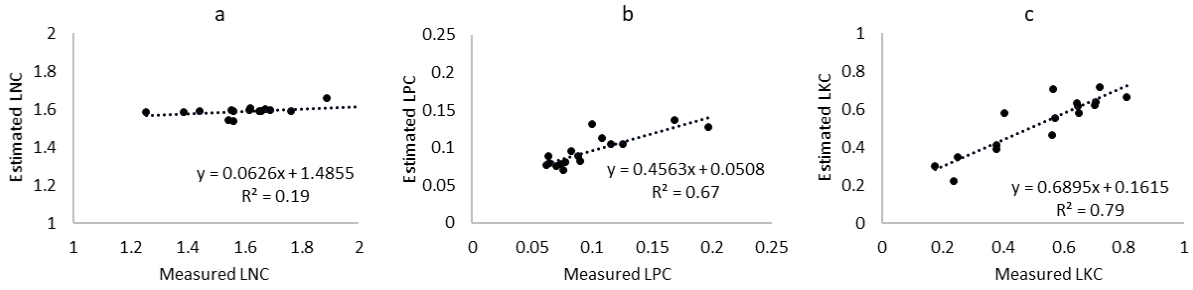

Fig. 14.- Linear regressions between LNC (a), LPC (b) and LKC (c) measured by chemical methods and those estimated values based on GPR.

4. Discussion

Many studies have demonstrated the suitability of spectral remote sensing for the detection of agronomic parameters, which provides information that will enable better crop management decisions across space and time (Curran, 1989; Maes & Steppe, 2019). The present study was aimed at developing a method for estimating the LNC, LPC and LKC from multispectral data acquired with an UAV under field conditions.

Up to now there have been numerous bibliographic references related to this particular topic. However, most of these publications have been centred only in N status for several crops (Lee et al., 2020; Perry et al., 2018; Yang et al., 2017), with other important nutrients scarcely discussed, especially for olive trees. In the present research, the results obtained for LNC estimation were worse than those showed for LPC and LKC. These results were expected, as the reflectance values for the five measured bands were similar regardless of the Nitrogen status of the olive trees (figure 9). Furthermore, the spectral range captured by the multispectral camera used (450-850 nm) only includes the spectral domains of VIS, red edge and NIR. This spectral range contains bands with a strong response to chlorophyll content, which is related to N status because of the large amount of protein that integrate this photosynthetic pigment (Muñoz-Huerta et al., 2013). Hence, a reduction in the plant N uptake induces a reduction of chlorophyll concentration in the leaves, which could turn them yellowish or reddish. Thus, deficiency in N concentration leads leaves to a shorter life, what increases canopy

porosity and tree exposure to the solar radiation, thus making them prone to sunburn (Sanzani, 2012). However, the linkage between chlorophyll content and LNC is weak in terms of the Pearson correlation coefficient, with values ranging 0.65 ± 0.15 across ecosystems (Homolová, Malenovský, Clevers, García-Santos, & Schaepman, 2013). This is due to there are several sources of N in the plant apart from chlorophyll. The ratio of plant's N content in form of chlorophyll may differ between species and depend on the growth stage of the plant. The interspecific differences depend on several factors. For example, the morphology of the leaves is determined by N allocation. Thus, the morphology of leaves may alter the relationship between N concentration in form of chlorophyll and total N plant content (Hikosaka, 2004). Additionally, there are others factors, not related to N status, that may alter the chlorophyll content such as: other nutritional deficiencies (sulphur deficiency) (Schnug & Haneklaus, 2005), rust infestation (Bravo, Moshou, West, McCartney, & Ramon, 2003), herbicide damage, freeze damage or moisture stress (Kimura, Bell, Trostle, Neely, & Drake, 2016). Thus, considering the chlorophyll content as a proxy for the plant N status can be misleading. These reasons may explain the better performance reached by (Lee et al., 2020) for LNC estimation in corn despite they employed a similar spectral range than the used in this study. Concretely, may be due to a better correlation between chlorophyll content and Nitrogen weight in corn than the one shown by olive trees.

Besides chlorophyll, N is an essential constituent of various enzymatic proteins that catalyse and regulate plant-growth processes. Thus, plant N uptake determines the potential protein content of plant tissues (Muñoz-Huerta et al., 2013). The reflectance spectra in the short-wave infrared (SWIR) spectral region (1100–2500 nm) is directly related to N-hydrogen (H) stretch, first overtone and absorption features of protein (Herrmann, Karnieli, Bonfil, Cohen, & Alchanatis, 2010). In this sense, several authors have shown improvements in N content estimations using this spectral region (Herrmann et al., 2010; Pandey et al., 2017). Therefore, since the spectral range of the sensor used (450-850 nm) only reaches the NIR domain, the discrete results obtained by all the proposed models in the case of LNC estimation, could be because the input data provided to the models were suboptimal for the intended purpose.

On the other hand, the results of LPC and LKC estimation were positive for the four proposed approaches. In the case of LPC estimation, the GPR approach yielded worse fits between the estimation and the measurement (R^2 = 0.67, RMSE = 0.024), followed by SVM (R^2 = 0.71, RMSE = 0.025), PLSR (R^2 = 0.80, RMSE = 0.017) and ANN (R^2 = 0.89, RMSE = 0.013). The results related to LKC estimation were even better, showing again the ANN approach the best response (R^2 = 0.93, RMSE = 0.059). SVM (R^2 = 0.80, RMSE = 0.101) and PLSR (R^2 = 0.80, RMSE = 0.115) had similar performances. And GPR (R^2 = 0.79, RMSE = 0.089) was slightly worse in terms of R^2 but showed a lesser value of RMSE. The overall variations in canopy spectra were affected by the variations in LPC and LKC rates. Generally, the olive trees with critical values of P or K showed a higher reflectance in the five captured bands. This fact, along with the goodness-of-fit observed between the response of the four evaluated models and the results of the chemical analysis indicated the relationship between the LPC and LKC and the spectral response in the five bands considered.

The function of P as energy supplier is a key factor in energy consumption processes such as plant photosynthesis. Photosynthesis performance determines leaf area and leaf biomass (Mahajan, Sahoo, Pandey, Gupta, & Kumar, 2014), and involves numerous structural organic compounds. Thereby, symptoms of P content deficiency are very similar to those of N deficiency, with trees showing reduced growth and yield. However, leaves look smaller but are not deformed or chlorotic as in the case of N deficiency (Sanzani, 2012). Furthermore, P is a constituent of nucleic acids and nucleoproteins, making it an omnipresent constituent of proteins (Y. J. Wang et al., 2020). On the other hand, K functions in buffering anions and in the regulation of cell pH. Moreover, K is involved in the activation of many enzymes in meristematic tissues and participates in protein synthesis and photosynthesis, as it plays an important role in chloroplasts formation and transportation of photosynthates. In addition, K is essential for the correct water balance in the plant since it is required for turgor build up and for maintaining the osmotic potential of cells, which in guard cells governs the opening of stomata. This confers K a decisive role in water uptake from the soil, water retention in the tissue and in the carriage of water and metabolites in the phloem and xylem (Y. J. Wang et al., 2020). Therefore, K plays an

important role in the regulation of water status in olive trees, which becomes more important considering the isohydric behaviour of this specie (Fernández, 2014). Symptoms of K deficiency in leaves involve a reduction of their size and chlorosis of tips and edges, that evolves into necrosis, which can be discerned with the appearance of a kind of 'burns' (Sanzani, 2012). For these reasons, although P and K may not have a direct influence in the spectral response, they could be indirectly detected through secondary effects related to their deficiencies or excesses, or by the related organic or complex compounds containing P or K elements in olive leaves.

To the best of our knowledge, most research aimed to develop non-destructive methods for plant nutrient status assessment based on spectral data have been focused on Nitrogen. In fact, most of the few publications focused on LPC and LKC estimation have been accomplished under laboratory conditions at leaf scale (Malmir et al., 2020; Pandey et al., 2017; Y. J. Wang et al., 2020; Zhang et al., 2013). All the mentioned studies used hyperspectral imaging system installed in laboratory which requires controlled lighting conditions and a previous sample collection. Unlike those, in the present study the spectral images were acquired under field conditions at canopy-scale by using an airborne platform, which avoids the necessity of collecting leaves samples and enables the coverage of large areas in a reduced time period with a high spatial resolution. On the other hand, these studies used hyperspectral imaging systems for spectral data collection which have an elevated spectral resolution. Instead of this, in the present study, a multispectral device with a spectral resolution of just five bands was used. It may seem a disadvantage, however the greater simplicity of the data facilitates the operation of mathematical models while reducing the noise and avoiding the necessity of wavelength selection. Furthermore, the lower cost of this type of devices must be highlighted. The results obtained in the present research, in the cases of LPC and LKC estimation, yielded a better fit than those published in the mentioned studies (Table 6). Considering the advantages of the proposed approach, the results obtained in this research take on greater importance.

Table 6

Summary of articles addressing the estimation of LNC, LPC or/and LKC in different crops by means of spectral data.

Reference	Crop	Nutrient	Regression Model	Prediction Accuracy (R^2)	Experimental conditions	Data
This work	Olive	N/P/K	ANN	0.63/0.89/0.93	Field	MSI*
(Malmir et al., 2020)	Cacao	N/P/K	PLSR	0.74/0.75/0.35	Laboratory	HSI*
(Pandey et al., 2017)	Maize and Soybean	N/P/K	PLSR	0.92/0.83/0.83	Laboratory	HSI
(Y. J. Wang et al., 2020)	Tea	P/K	MLR*	0.94/0.92	Laboratory	HSI
(Zhang et al., 2013)	Rape	N/P/K	LS-SVM*	0.88/0.71/0.75	Laboratory	HSI

* MLR, multiple linear regression. *LS-SVM, least-squares support vector machines. *HSI, hyperspectral imaging system. *MSI, multispectral imaging system.

Another interesting result of this work includes the different performance of the evaluated retrieval methods. The best performance of the ANN approach was reached with just one hidden layer and a unique neuron. It indicated that the relationship between the spectral information considered and the LPC and LKC would approach linearity. However, the ANN approach showed better results than the techniques based on linear regression (PLSR). It probably was due to the higher flexibility of the ANN approach, due to the nonlinearity of the sigmoid output lay. This fact allowed ANN to adjust more effectively to the feature space (Verrelst et al., 2012). Numerous studies have demonstrated the superiority of ANNs in vegetation properties mapping compared to parametric models (Kalacska, Lalonde, & Moore, 2015; F. Wang et al., 2013). On the other hand, previous works have informed about the superiority of ANN approaches against linear nonparametric models (PLSR) (Huang, Turner, Dury, Wallis, & Foley, 2004; Jensen, Hardin, & Hardin, 2012). A common disadvantage of ANN models is that they are prone to overfitting. It occurs when the models learn random fluctuations and noise from the training data in high detail. Hence, performance and generalization capability of the trained models is adversely affected. However, problems of overfitting are generally applicable to machine learning models. Furthermore, in the present study the validation data sets were completely independent of

737 the training sets, so it would be improbable that overfitting-induced mistakes were the reason for the
738 high correlation between the validation set and the response of the ANN model.

739 Another important contribution of this research to the state of the art is the proposed image
740 processing methodology. This allows the overlapping of the multispectral image sets for generating
741 orthomosaic maps, which cover the whole orchard. Furthermore, the proposed methodology enables
742 the automatic segmentation of olive trees. This feature makes possible to discard the background
743 information, which results in a better performance of the retrieval methods as a lot of unnecessary
744 information is avoiding. In addition to all the above, the proposed image processing methodology
745 offers the possibility of acquired information from discrete points, giving to the method a very high
746 spatial resolution.

747 **5. Conclusions**

748 The present work was aimed at exploring the viability of the development of a new method for olive
749 nutrient status assessment, by using affordable equipment directly operating under field conditions.
750 To that end, an approach based on the analysis of multispectral imagery acquired with an UAV was
751 proposed. An important obstacle towards this goal was the strategy to obtain spectral data from an
752 aerial perspective. To solve this issue, a new image processing approach was developed to integrate
753 all the spectral images acquired during the flights in single orthomosaics. This image analysis
754 methodology automatically discards the background information and enables the autonomous
755 extraction of data from discrete points. This approach was evaluated in an experimental super
756 intensive olive orchard. Several retrieval techniques (PLSR, ANN, SVR and GPR) were evaluated for LNC,
757 LPC and LKC estimation by using the five-reflectance data extracted from the multispectral
758 orthomosaics as input variables and the results of chemical analyses as reference.

759 The obtained results showed the suitability of the proposed image processing approach and indicate
760 the ANN as the best retrieval technique for these experimental conditions. Although the results were

promising, further work is needed to expand the experimental setup to different environmental conditions, olive varieties and plant vegetative stages.

However, the higher spatial and temporal resolution compared against the current methods, paves the way for the implementation of an olive orchard nutrient status appraisal system. These technical improvements could create new paths in sustainable oliviculture, enabling the deployment of solutions for automatic and continuous evaluation of fertilizers needs, which will enable a more precise and efficient fertirrigation programs design. Consequently, it would increase the olive orchard productivity and profitability, improving the economy of the olive sector and encouraging a more sustainable agriculture.

Author Contributions: J.M.A., A.C., J.S., R.C., M.E.M., and P.J. conceived and directed the experimental layout. A.C., J.S., R.C., M.E.M., and P.J designed and developed the plant-based variables acquisition. A.A. and J.M.P. designed and developed the flight execution and the Image processing methodology. M.N. and A.A. designed and developed the methodology for nutritional status estimation from multispectral information. M.N. and A.A. drafted the manuscript , which was revised and edited by J.M.A. All authors read and approved the final manuscript.

Funding: The research and APC were funded by the Interreg Cooperation Program V-A SPAIN-PORTUGAL (POCTEP) 2014–2020 and co-financed with ERDF (European Regional Development Fund), grant number 0155_TECNOLIVO_6_E, within the scope of the TecnOlivo Project.

6. References

Ali, M. M., Al-Ani, A., Eamus, D., & Tan, D. K. Y. (2017). Leaf nitrogen determination using non-destructive techniques–A review. *Journal of Plant Nutrition*, *40*(7), 928–953. https://doi.org/10.1080/01904167.2016.1143954

Barranco Navero, Diego, Fernandez Escobar, Ricardo, Rallo Romero, L. (2017). *El cultivo del olivo* (7ª ed; Mundi-Prensa Libros, ed.). Retrieved from

785 https://books.google.es/books?hl=es&lr=&id=hWFIDgAAQBAJ&oi=fnd&pg=PR4&dq=el+cultivo+
786 del+olivo+&ots=mIHZNUIKeI&sig=bkqNNc3clxUVVWydyGVsteBF91M#v=onepage&q=el cultivo
787 del olivo&f=false

788 Barzin, R., Pathak, R., Lotfi, H., Varco, J., & Bora, G. C. (2020). Use of UAS multispectral imagery at
789 different physiological stages for yield prediction and input resource optimization in corn.
790 *Remote Sensing*, *12*(15), 2392. https://doi.org/10.3390/RS12152392

791 Berger, K., Verrelst, J., Féret, J. B., Wang, Z., Wocher, M., Strathmann, M., … Hank, T. (2020, June 1).
792 Crop nitrogen monitoring: Recent progress and principal developments in the context of
793 imaging spectroscopy missions. *Remote Sensing of Environment*, Vol. 242, p. 111758.
794 https://doi.org/10.1016/j.rse.2020.111758

795 Bindraban, P. S., Dimkpa, C., Nagarajan, L., Roy, A., & Rabbinge, R. (2015, November 1). Revisiting
796 fertilisers and fertilisation strategies for improved nutrient uptake by plants. *Biology and*
797 *Fertility of Soils*, Vol. 51, pp. 897–911. https://doi.org/10.1007/s00374-015-1039-7

798 Bravo, C., Moshou, D., West, J., McCartney, A., & Ramon, H. (2003). Early disease detection in wheat
799 fields using spectral reflectance. *Biosystems Engineering*, *84*(2), 137–145.
800 https://doi.org/10.1016/S1537-5110(02)00269-6

801 Calderón, R., Navas-Cortés, J. A., Lucena, C., & Zarco-Tejada, P. J. (2013). High-resolution airborne
802 hyperspectral and thermal imagery for early detection of Verticillium wilt of olive using
803 fluorescence, temperature and narrow-band spectral indices. *Remote Sensing of Environment*,
804 *139*, 231–245. https://doi.org/10.1016/j.rse.2013.07.031

805 Camino, C., González-Dugo, V., Hernández, P., Sillero, J. C., & Zarco-Tejada, P. J. (2018). Improved
806 nitrogen retrievals with airborne-derived fluorescence and plant traits quantified from VNIR-
807 SWIR hyperspectral imagery in the context of precision agriculture. *International Journal of*
808 *Applied Earth Observation and Geoinformation*, *70*, 105–117.

https://doi.org/10.1016/j.jag.2018.04.013

Camps-Valls, G., Verrelst, J., Munoz-Mari, J., Laparra, V., Mateo-Jimenez, F., & Gomez-Dans, J. (2016). A survey on Gaussian processes for earth-observation data analysis: A comprehensive investigation. *IEEE Geoscience and Remote Sensing Magazine*, *4*(2), 58–78. https://doi.org/10.1109/MGRS.2015.2510084

Caruso, G., Zarco-Tejada, P. J., González-Dugo, V., Moriondo, M., Tozzini, L., Palai, G., … Gucci, R. (2019). High-resolution imagery acquired from an unmanned platform to estimate biophysical and geometrical parameters of olive trees under different irrigation regimes. *PLoS ONE*, *14*(1), 1–19. https://doi.org/10.1371/journal.pone.0210804

Chaves, E. S., dos Santos, E. J., Araujo, R. G. O., Oliveira, J. V., Frescura, V. L. A., & Curtius, A. J. (2010). Metals and phosphorus determination in vegetable seeds used in the production of biodiesel by ICP OES and ICP-MS. *Microchemical Journal*, *96*(1), 71–76. https://doi.org/10.1016/j.microc.2010.01.021

Curran, P. J. (1989). Remote sensing of foliar chemistry. *Remote Sensing of Environment*, *30*(3), 271–278. https://doi.org/10.1016/0034-4257(89)90069-2

Duarte, L., Pacheco, C., & Soveral-Dias, J. C. (1998). *Métodos de análise de material vegetal*. Lisboa: INIAV/LQARS.

FAOSTAT. (2020). Retrieved October 15, 2020, from http://www.fao.org/faostat/en/#data/RFN/visualize

Fernández-Escobar, R., Beltrán, G., Sánchez-Zamora, M. A., García-Novelo, J., Aguilera, M. P., & Uceda, M. (2006). Olive oil quality decreases with nitrogen over-fertilization. *HortScience*, *41*(1), 215–219. https://doi.org/10.21273/hortsci.41.1.215

Fernández-Escobar, R., Marin, L., Sánchez-Zamora, M. A., García-Novelo, J. M., Molina-Soria, C., & Parra, M. A. (2009). Long-term effects of N fertilization on cropping and growth of olive trees

and on N accumulation in soil profile. *European Journal of Agronomy*, *31*(4), 223–232. https://doi.org/10.1016/j.eja.2009.08.001

Fernández-Escobar, Ricardo. (2019). Olive Nutritional Status and Tolerance to Biotic and Abiotic Stresses. *Frontiers in Plant Science*, *10*(September), 1–7. https://doi.org/10.3389/fpls.2019.01151

Fernández-Escobara, R. (2018). Trends in olive nutrition. *Acta Horticulturae*, *1199*, 215–223. https://doi.org/10.17660/ActaHortic.2018.1199.35

Fernández, J. E. (2014). Understanding olive adaptation to abiotic stresses as a tool to increase crop performance. *Environmental and Experimental Botany*, *103*, 158–179. https://doi.org/10.1016/j.envexpbot.2013.12.003

Geladi, P., & Kowalski, B. R. (1986). Partial least-squares regression: a tutorial. *Analytica Chimica Acta*, *185*(C), 1–17. https://doi.org/10.1016/0003-2670(86)80028-9

Gómez-Casero, M. T., López-Granados, F., Peña-Barragán, J. M., Jurado-Expósito, M., García-Torres, L., & Fernández-Escobar, R. (2007). Assessing nitrogen and potassium deficiencies in olive orchards through discriminant analysis of hyperspectral data. *Journal of the American Society for Horticultural Science*, *132*(5), 611–618. https://doi.org/10.21273/jashs.132.5.611

Gonzalez-Dugo, V., Zarco-Tejada, P., Nicolás, E., Nortes, P. A., Alarcón, J. J., Intrigliolo, D. S., & Fereres, E. (2013). Using high resolution UAV thermal imagery to assess the variability in the water status of five fruit tree species within a commercial orchard. *Precision Agriculture*, *14*(6), 660–678. https://doi.org/10.1007/s11119-013-9322-9

Hank, T. B., Berger, K., Bach, H., Clevers, J. G. P. W., Gitelson, A., Zarco-Tejada, P., & Mauser, W. (2019, May 1). Spaceborne Imaging Spectroscopy for Sustainable Agriculture: Contributions and Challenges. *Surveys in Geophysics*, Vol. 40, pp. 515–551. https://doi.org/10.1007/s10712-018-9492-0

857 Herrmann, I., Karnieli, A., Bonfil, D. J., Cohen, Y., & Alchanatis, V. (2010). SWIR-based spectral indices
858 for assessing nitrogen content in potato fields. *International Journal of Remote Sensing*, *31*(19),
859 5127–5143. https://doi.org/10.1080/01431160903283892

860 Hikosaka, K. (2004, December 2). Interspecific difference in the photosynthesis-nitrogen relationship:
861 Patterns, physiological causes, and ecological importance. *Journal of Plant Research*, Vol. 117,
862 pp. 481–494. https://doi.org/10.1007/s10265-004-0174-2

863 Homolová, L., Malenovský, Z., Clevers, J. G. P. W., García-Santos, G., & Schaepman, M. E. (2013,
864 September 1). Review of optical-based remote sensing for plant trait mapping. *Ecological*
865 *Complexity*, Vol. 15, pp. 1–16. https://doi.org/10.1016/j.ecocom.2013.06.003

866 Huang, Z., Turner, B. J., Dury, S. J., Wallis, I. R., & Foley, W. J. (2004). Estimating foliage nitrogen
867 concentration from HYMAP data using continuum removal analysis. *Remote Sensing of*
868 *Environment*, *93*(1–2), 18–29. https://doi.org/10.1016/j.rse.2004.06.008

869 Jensen, R. R., Hardin, P. J., & Hardin, A. J. (2012). Estimating urban leaf area index (LAI) of individual
870 trees with hyperspectral data. *Photogrammetric Engineering and Remote Sensing*, *78*(5), 495–
871 504. https://doi.org/10.14358/PERS.78.5.495

872 Kalacska, M., Lalonde, M., & Moore, T. R. (2015). Estimation of foliar chlorophyll and nitrogen
873 content in an ombrotrophic bog from hyperspectral data: Scaling from leaf to image. *Remote*
874 *Sensing of Environment*, *169*, 270–279. https://doi.org/10.1016/j.rse.2015.08.012

875 Kimura, E., Bell, J., Trostle, C., Neely, C., & Drake, D. (2016). Yellowing of younger leaves without
876 interveinal chlorosis: S deficiency. In *The Texas A&M University System, U.S. Department of*
877 *Agriculture*. Retrieved from http://amarillo.tamu.

878 Lee, H., Wang, J., & Leblon, B. (2020). Using Linear Regression, Random Forests, and Support Vector
879 Machine with Unmanned Aerial Vehicle Multispectral Images to Predict Canopy Nitrogen
880 Weight in Corn. *Remote Sensing*, *12*(13), 2071. https://doi.org/10.3390/rs12132071

881 Lemaire, G., Jeuffroy, M. H., & Gastal, F. (2008). Diagnosis tool for plant and crop N status in
882 vegetative stage. Theory and practices for crop N management. *European Journal of Agronomy*,
883 *28*(4), 614–624. https://doi.org/10.1016/j.eja.2008.01.005

884 Li, D., Li, C., Yao, Y., Li, M., & Liu, L. (2020, July 1). Modern imaging techniques in plant nutrition
885 analysis: A review. *Computers and Electronics in Agriculture*, Vol. 174, p. 105459.
886 https://doi.org/10.1016/j.compag.2020.105459

887 Liu, H., Zhu, H., & Wang, P. (2017). Quantitative modelling for leaf nitrogen content of winter wheat
888 using UAV-based hyperspectral data. *International Journal of Remote Sensing*, *38*(8–10), 2117–
889 2134. https://doi.org/10.1080/01431161.2016.1253899

890 López-Granados, F., Jurado-Expósito, M., Álamo, S., & García-Torres, L. (2004). Leaf nutrient spatial
891 variability and site-specific fertilization maps within olive (Olea europaea L.) orchards. *European*
892 *Journal of Agronomy*, *21*(2), 209–222. https://doi.org/10.1016/j.eja.2003.08.005

893 Maes, W. H., & Steppe, K. (2019, February 1). Perspectives for Remote Sensing with Unmanned Aerial
894 Vehicles in Precision Agriculture. *Trends in Plant Science*, Vol. 24, pp. 152–164.
895 https://doi.org/10.1016/j.tplants.2018.11.007

896 Mahajan, G. R., Sahoo, R. N., Pandey, R. N., Gupta, V. K., & Kumar, D. (2014). Using hyperspectral
897 remote sensing techniques to monitor nitrogen, phosphorus, sulphur and potassium in wheat
898 (Triticum aestivum L.). *Precision Agriculture*, *15*(5), 499–522. https://doi.org/10.1007/s11119-
899 014-9348-7

900 Malmir, M., Tahmasbian, I., Xu, Z., Farrar, M. B., & Bai, S. H. (2020). Prediction of macronutrients in
901 plant leaves using chemometric analysis and wavelength selection. *Journal of Soils and*
902 *Sediments*, *20*(1), 249–259. https://doi.org/10.1007/s11368-019-02418-z

903 Mondino, E. B. (2018). Remote Sensing from RPAS in Agriculture: An Overview of Expectations and
904 Unanswered Questions. *Mechanisms and Machine Science*, *49*(June), 797–804.

https://doi.org/10.1007/978-3-319-61276-8

Morlini, I. (2006). On multicollinearity and concurvity in some nonlinear multivariate models. *Statistical Methods and Applications*, *15*(1), 3–26. https://doi.org/10.1007/s10260-006-0005-9

Muñoz-Huerta, R. F., Guevara-Gonzalez, R. G., Contreras-Medina, L. M., Torres-Pacheco, I., Prado-Olivarez, J., & Ocampo-Velazquez, R. V. (2013). A review of methods for sensing the nitrogen status in plants: Advantages, disadvantages and recent advances. *Sensors (Switzerland)*, *13*(8), 10823–10843. https://doi.org/10.3390/s130810823

Pandey, P., Ge, Y., Stoerger, V., & Schnable, J. C. (2017). High throughput in vivo analysis of plant leaf chemical properties using hyperspectral imaging. *Frontiers in Plant Science*, *8*(August), 1–12. https://doi.org/10.3389/fpls.2017.01348

Park, S., Ryu, D., Fuentes, S., Chung, H., Hernández-Montes, E., & O'Connell, M. (2017). Adaptive Estimation of Crop Water Stress in Nectarine and Peach Orchards Using High-Resolution Imagery from an Unmanned Aerial Vehicle (UAV). *Remote Sensing*, *9*(8), 828. https://doi.org/10.3390/rs9080828

Pasolli, L., Melgani, F., & Blanzieri, E. (2010). Gaussian process regression for estimating chlorophyll concentration in subsurface waters from remote sensing data. *IEEE Geoscience and Remote Sensing Letters*, *7*(3), 464–468. https://doi.org/10.1109/LGRS.2009.2039191

Perry, E. M., Goodwin, I., & Cornwall, D. (2018). Remote sensing using canopy and leaf reflectance for estimating nitrogen status in red-blush pears. *HortScience*, *53*(1), 78–83. https://doi.org/10.21273/HORTSCI12391-17

Saberioon, M., Amin, M. S. M., Gholizadeh, A., & Ezri, M. H. (2014). A review of optical methods for assessing nitrogen contents during rice growth. *Applied Engineering in Agriculture*, *30*(4), 657–669. https://doi.org/10.13031/aea.30.10478

Sanzani, S. M. (2012). ABIOTIC DISEASES OF OLIVE. *Journal of Plant Pathology*, *94*(3), 469–491.

Retrieved from https://www.jstor.org/stable/45156275?seq=1#metadata_info_tab_contents

Savci, S. (2012). An Agricultural Pollutant: Chemical Fertilizer. *International Journal of Environmental Science and Development*, *3*(1), 73–80. https://doi.org/10.7763/ijesd.2012.v3.191

Schnug, E., & Haneklaus, S. (2005, September 1). Sulphur deficiency symptoms in oilseed rape (Brassica napus L.) - The aesthetics of starvation. *Phyton - Annales Rei Botanicae*, Vol. 45, pp. 79–95.

Soille, P. (2004). *Morphological Image Analysis : Principles and Applications*. 391.

Sui, R., Wilkerson, J. B., Hart, W. E., Wilhelm, L. R., & Howard, D. D. (2005). *MULTI–SPECTRAL SENSOR FOR DETECTION OF NITROGEN STATUS IN COTTON*. *21*(2), 167–172.

Thompson, M. (2012). *Handbook of Inductively Coupled Plasma Spectrometry: Second Edition* (2nd ed; S. S. & B. Media, Ed.). Retrieved from https://books.google.es/books?hl=es&lr=&id=8psyBwAAQBAJ&oi=fnd&pg=PT10&dq=Handbook+of+inductively+coupled+plasma+spectrometry&ots=pdvV_ihIUW&sig=R2gTw6WTIhXrigQPhPA9Zjrsdz4#v=onepage&q=Handbook of inductively coupled plasma spectrometry&f=false

Tremblay, N., Fallon, E., & Ziadi, N. (2011). Sensing of crop nitrogen status: Opportunities, tools, limitations, and supporting information requirements. *HortTechnology*, *21*(3), 274–281.

Verrelst, J., Malenovský, Z., Van der Tol, C., Camps-Valls, G., Gastellu-Etchegorry, J. P., Lewis, P., … Moreno, J. (2019, May 1). Quantifying Vegetation Biophysical Variables from Imaging Spectroscopy Data: A Review on Retrieval Methods. *Surveys in Geophysics*, Vol. 40, pp. 589–629. https://doi.org/10.1007/s10712-018-9478-y

Verrelst, J., Muñoz, J., Alonso, L., Delegido, J., Rivera, J. P., Camps-Valls, G., & Moreno, J. (2012). Machine learning regression algorithms for biophysical parameter retrieval: Opportunities for Sentinel-2 and -3. *Remote Sensing of Environment*, *118*, 127–139. https://doi.org/10.1016/j.rse.2011.11.002

Vogel, A. I. (1978). *Vogel's Textbook of quantitative inorganic analysis* (4th Ed; Longman, Ed.). Londres.

Wang, F., Huang, J., Wang, Y., Liu, Z., Peng, D., & Cao, F. (2013). Monitoring nitrogen concentration of oilseed rape from hyperspectral data using radial basis function. *International Journal of Digital Earth*, *6*(6), 550–562. https://doi.org/10.1080/17538947.2011.628414

Wang, Y. J., Jin, G., Li, L. Q., Liu, Y., Kianpoor Kalkhajeh, Y., Ning, J. M., & Zhang, Z. Z. (2020). NIR hyperspectral imaging coupled with chemometrics for nondestructive assessment of phosphorus and potassium contents in tea leaves. *Infrared Physics and Technology*, *108*. https://doi.org/10.1016/j.infrared.2020.103365

Wold, S., Sjöström, M., & Eriksson, L. (2001). PLS-regression: A basic tool of chemometrics. *Chemometrics and Intelligent Laboratory Systems*, *58*(2), 109–130. https://doi.org/10.1016/S0169-7439(01)00155-1

Yang, G., Liu, J., Zhao, C., Li, Z., Huang, Y., Yu, H., … Yang, H. (2017, June 30). Unmanned aerial vehicle remote sensing for field-based crop phenotyping: Current status and perspectives. *Frontiers in Plant Science*, Vol. 8, p. 1111. https://doi.org/10.3389/fpls.2017.01111

Zhang, X., Liu, F., He, Y., & Gong, X. (2013). Detecting macronutrients content and distribution in oilseed rape leaves based on hyperspectral imaging. *Biosystems Engineering*, *115*(1), 56–65. https://doi.org/10.1016/j.biosystemseng.2013.02.007